

**Copyright
by
Ryan Patrick Hannigan
2023**

The Dissertation Committee for Ryan Patrick Hannigan certifies that
this is the approved version of the following dissertation:

Stranger Things at the LHC

Committee:

Christina Markert, Supervisor

Peter Onyisi

Richard Hazeltine

Chandrajit Bajaj

Stranger Things at the LHC

by

Ryan Patrick Hannigan, B.S.

Dissertation

Presented to the Faculty of the Graduate School of
The University of Texas at Austin
in Partial Fulfillment
of the Requirements
for the degree of
Doctor of Philosophy

The University of Texas at Austin
May, 2023

To Jaynee, who unquestionably is the reason why this document exists.

Stranger Things at the LHC

Publication No. _____

Ryan Patrick Hannigan, Ph.D.
The University of Texas at Austin, 2023

Supervisor: Christina Markert

Among the most mysterious of the four fundamental forces is the strong nuclear force. Responsible for both the binding together of nucleons within an atom, as well as the

Contents

List of Figures	viii
List of Tables	xii
Chapter One: Introduction	1
1.1 What is fundamental?	1
Chapter Two: Experimental Apparatus	5
2.1 The LHC	5
2.2 The ALICE Detector	6
Chapter Three: Analysis Details	10
3.1 Dataset and event selection	10
3.2 Charged hadron track selection	11
3.3 Λ reconstruction	13
3.4 Reconstruction efficiency	20
3.5 Corrections to the correlation distributions	23
Chapter Four: Systematic uncertainties and cross-checks	38
4.1 Systematic uncertainties	38
Bibliography	55

List of Figures

1.1	A diagram depicting the particles we currently believe are fundamental within the so-called “Standard Model” of particle physics.	2
1.2	A coffee cup with the Standard Model Lagrangian density printed on its side. Please ignore the “+ h.c.” term following the $i\bar{\psi}\not{D}\psi$, it is the result of a small lapse in judgement from the mug makers.	3
2.1	A diagram depicting the LHC with its various main detectors shown underground. Illustration by Phillippe Mouche, from BBC News.	6
2.2	A 3-D schematic of the ALICE detector, with labels for all of the sub-detectors. Note the humans-for-scale in the bottom left of the diagram. .	7
3.1	The p_T (left), φ (middle) and η (right) distributions for the trigger hadrons in the multiplicity range 0-20%.	12
3.2	The p_T (left), φ (middle) and η (right) distributions for the associated hadrons in the multiplicity range 0-20%. The dips observed in the φ distribution are due to the TPC sector boundaries.	13
3.3	A diagram depicting a typical V^0 decay with labels for the most important kinematic variables. The diagram was taken from [10].	14
3.4	$n\sigma$ for protons (left) and pions (right) in the TPC detector as a function of p_T	16
3.5	$n\sigma$ for protons (left) and pions (right) in the TOF detector as a function of p_T	16
3.6	$n\sigma$ in TOF vs $n\sigma$ in TPC for protons (left) and pions (right). No continuation is observed for both of the particle species.	17
3.7	Invariant mass distributions in the 0-20% (top), 20-50% (middle), and 50-80% (bottom) multiplicity bins for the Λ candidates which pass the selection criteria with $1.5 < p_T < 2.5 \text{ GeV}/c$ (left) and $2.5 < p_T < 4.0 \text{ GeV}/c$ (right). A Voigtian signal + straight-line background fit to the data is shown in blue, with just the background fit shown in red. For these plots, the Λ s were only reconstructed in events with a trigger hadron.	19

3.8	Efficiency vs. p_T for trigger (left) and associated (right) hadrons. While they may look identical, the associated hadron efficiency is slightly lower due to the stricter selection criteria.	21
3.9	Efficiency vs. p_T (left) and η (right) for Λ reconstruction in each multiplicity bin, along with an integrated 0-100% point in red.	22
3.10	2-D non-acceptance corrected h- Λ angular correlations for the 0-20% (top), 20-50% (middle), and 50-80% (bottom) multiplicity bins for $1.5 < p_T < 2.5 \text{ GeV}/c$ (left) and $2.5 < p_T < 4.0 \text{ GeV}/c$ (right).	25
3.11	2-D non-acceptance corrected h-h angular correlations for the 0-20% (top), 20-50% (middle), and 50-80% (bottom) multiplicity bins for $1.5 < p_T < 2.5 \text{ GeV}/c$ (left) and $2.5 < p_T < 4.0 \text{ GeV}/c$ (right).	26
3.12	2-D mixed-event h- Λ angular correlations for the 0-20% (top), 20-50% (middle), and 50-80% (bottom) multiplicity bins for $1.5 < p_T < 2.5 \text{ GeV}/c$ (left) and $2.5 < p_T < 4.0 \text{ GeV}/c$ (right). The Z_{vtx} . bins are merged together for these plots.	27
3.13	2-D mixed-event h-h angular correlations for the 0-20% (top), 20-50% (middle), and 50-80% (bottom) multiplicity bins for $1.5 < p_T < 2.5 \text{ GeV}/c$ (left) and $2.5 < p_T < 4.0 \text{ GeV}/c$ (right). The Z_{vtx} . bins are merged together for these plots.	28
3.14	Invariant mass distribution of $p\pi$ pairs in the 20-50% multiplicity class. The signal region is shown in light green, and the sideband region is shown in light pink. The correlation distribution in the sideband region is used to remove the combinatorial background from the signal region.	30
3.15	The signal (top) and sideband (bottom) distributions $C_{\text{signal}}^{\text{h-p}\pi}$ and $C_{\text{SB}}^{\text{h-p}\pi}$ for the lower (left) and higher (right) associated p_T bins. All plots were generated in the 0-20% multiplicity class.	31
3.16	Demonstration of the track merging effect for h- Λ pairs, whereby we see a dip in the reconstructed distribution at small $\Delta\varphi$ and $\Delta\eta$ when compared to the MC ground truth (left). This dip is not present at large $\Delta\eta$ (right), but we also lose nearly the entirety of our near-side peak.	33
3.17	The reconstructed/ground truth ratios of the 2D $C(\Delta\varphi, \Delta\eta)$ distributions for h-(secondary pions) (left) and h-(primary pions) (right). The suppression at smaller $\Delta\varphi, \Delta\eta$ is clearly seen in the secondary case, but is not observable in the primary case, indicating a decay-length dependence.	34

3.18 The reconstructed and ground truth $\Delta\varphi$ distributions in the $-1.2 < \Delta\eta < 1.2$ region for h-(secondary pions) with $0.15 < p_T < 2$ (left) and $2 < p_T < 4$ (right). The suppression at smaller $\Delta\eta, \Delta\varphi$ is clearly seen in the higher momentum bin, but not present in the lower one.	35
3.19 The $\epsilon_{\text{pair}}(\Delta\varphi, \Delta\eta)$ templates for the track merging correction in the lower ($1.5 < p_T < 2.5$ GeV/c, left) and higher ($2.5 < p_T < 4.0$ GeV/c, right) associated momentum bins. While it may be difficult to observe, the lower p_T bin has a minimum dip of around 0.84, whereas the higher p_T bin has a minimum dip of around 0.81, reflecting the p_T dependence discussed in this section.	37
4.1 The h- Λ $\Delta\varphi$ distributions within the 0-20% (top), 20-50% (middle) and 50-80% (bottom) multiplicity bins in the lower associated p_T bin for each of the signal region variations (left) with the ratios to the nominal distribution (right).	43
4.2 The h- Λ $\Delta\varphi$ distributions within the 0-20% (top), 20-50% (middle) and 50-80% (bottom) multiplicity bins in the higher associated p_T bin for each of the signal region variations (left) with the ratios to the nominal distribution (right).	44
4.3 The h- Λ $\Delta\varphi$ distributions within the 0-20% (top), 20-50% (middle) and 50-80% (bottom) multiplicity bins in the lower associated p_T bin for each of the sideband region variations (left) with the ratios to the nominal distribution (right).	45
4.4 The h- Λ $\Delta\varphi$ distributions within the 0-20% (top), 20-50% (middle) and 50-80% (bottom) multiplicity bins in the higher associated p_T bin for each of the sideband region variations (left) with the ratios to the nominal distribution (right).	46
4.5 The h- Λ $\Delta\varphi$ distributions within the 0-20% (top), 20-50% (middle) and 50-80% (bottom) multiplicity bins in the lower associated p_T bin for each of the PID cut variations (left) with the ratios to the nominal distribution (right).	47
4.6 The h- Λ $\Delta\varphi$ distributions within the 0-20% (top), 20-50% (middle) and 50-80% (bottom) multiplicity bins in the higher associated p_T bin for each of the PID cut variations (left) with the ratios to the nominal distribution (right).	48

4.7 Barlow check for the signal (left), sideband (middle), and PID (right) variations in the 0-20% multiplicity bin. The red lines represent $N\sigma_{RB} = \pm 1$, and if the majority of the points fall within the red lines (across all $\Delta\varphi$, multiplicity and p_T bins), they are excluded from the systematic uncertainty calculation.	49
4.8 A visual depiction of the final systematic errors for the $h-\Lambda$ $\Delta\varphi$ distributions for each multiplicity bin in the low (left) and high (right) associated p_T bins. The total systematic error is shown in black.	51
4.9 Visual depiction of the multiplicity-uncorrelated systematic errors for the $h-\Lambda$ $\Delta\varphi$ distributions for each multiplicity bin in the low (left) and high (right) associated p_T bins, along with the total systematic error shown in black.	52

List of Tables

3.1 Number of events passing our criteria for each multiplicity bin considered. Here Z_{vtx} refers to the position of the PV along the beam (z) axis.	11
3.2 The track quality cuts applied to the trigger hadrons in this analysis.	12
3.3 The ALICE standard track quality cuts for primary charged hadrons, used for the selection of the associated hadrons in this analysis.	13
3.4 The track quality cuts applied to both the daughter proton and pion tracks used to reconstruct Λ candidates. These cuts are intentionally less strict than those applied to the trigger and associated hadrons as the daughter tracks are reconstructed from secondary particles.	15
3.5 Topological selection criteria applied to Λ candidates.	18
4.1 The systematic uncertainties for the $\Delta\varphi$ distributions which are not di- rectly calculated in this thesis, instead taken from previous analyses using the same particle species and collision system [15], [17]–[19]. Each source of uncertainty is verified to be independent of multiplicity, but the Λ material budget and topological selection uncertainties exhibit a small dependence on p_T	40
4.2 The variations of the Λ invariant mass signal region considered for this analysis.	41
4.3 The variations of the Λ invariant mass sideband region considered for this analysis. Note that the “shifted left” sideband falls on the opposite (left) side of the signal region.	42
4.4 The variations of the Λ daughter PID cuts considered for this analysis. The “require TOF” variation requires a TOF hit for both the proton and pion, but maintains the nominal values for $ n\sigma_{\text{TPC, TOF}} $	42
4.5 The final systematic uncertainties (in percentages) from the h- Λ $\Delta\varphi$ dis- tribution generation for each multiplicity and associated p_T bin.	50
4.6 v_2 values used in this analysis for each $p_{T,\text{assoc}}$ bin.	53

Chapter One: Introduction

The purpose of this chapter is to transform a scientifically literate reader who may be vaguely familiar with the idea of a “quark” into one who can understand the motivation and techniques behind the analysis presented in the rest of this thesis. If you are an extremely educated physicist who regularly performs lattice quantum chromodynamics calculations in their head, I would also encourage you to read this chapter it its entirety as it may contain egregious errors that need to be corrected.

1.1 What is fundamental?

The answer to the question “What are the fundamental building blocks of our universe?” has changed drastically over the course of human history. The idea that all matter is composed of smaller, uncuttable pieces has been around since 5th century BCE when Greek philosophers Democritus and Leucippus first introduced the concept of an atom [1]. While this idea was mostly motivated by philosophical reasoning, it was later adopted by the English scientist John Dalton in the 19th century to explain the results of his chemical experiments, where he found that chemical elements always combined with each other by discrete units of mass [2]. However, everything changed around the turn of the 20th century when scientists like Rutherford and Chadwick determined that the supposedly indivisible atom was composed of even smaller particles, eventually named protons and neutrons [3], [4]. The notion that protons and neutrons were unbreakable was relatively short lived, as not even half a century later the deep inelastic scattering experiments performed by Kendall, Friedman and Taylor [5]–[7] revealed that protons (and subsequently neutrons) were actually composed of even smaller particles, eventually dubbed “partons”. [8]. This discovery was one of the largest contributing factors to the creation of the so-called Standard Model of particle physics, a theory which describes all of the fundamental particles and the way in which they interact with each other. A diagram of those fundamental particles can be seen in Figure 1.1. It should be noted that all of the particles labeled as quarks and leptons – collectively as “fermions” – have corresponding anti-particles with opposite electric charge. The equation that describes all of these

Standard Model of Elementary Particles

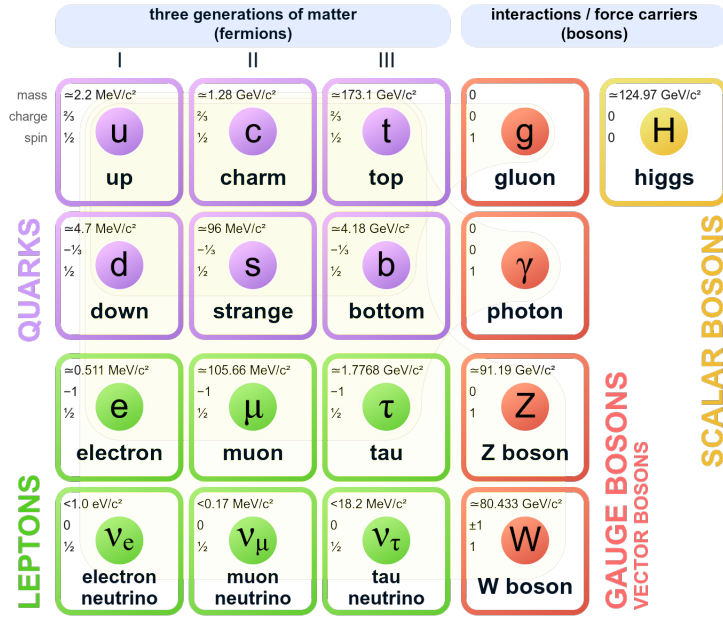


Figure 1.1: A diagram depicting the particles we currently believe are fundamental within the so-called “Standard Model” of particle physics.

particles and their interactions, often incorrectly¹ referred to as the “Standard Model Lagrangian”, can be compactified into a relatively palatable form that can easily fit on a coffee cup like the one shown in Figure 1.2.

While this equation may appear brief¹, it can be used to completely describe three of the four fundamental forces of nature:

1. The Electromagnetic Force, which is responsible for the electrons pushing against each other to keep you from falling through your chair,
2. The Weak Nuclear Force, which is responsible for the initiating the nuclear fusion reactions that fuel our sun, and

¹It is “incorrect” because this is technically a Lagrangian density (i.e. Lagrangian per unit volume), but as it is usually integrated over all space the distinction is mostly irrelevant.

¹Here “brief” is in the eye of the beholder, but certainly its brevity is misleading as even in the first line the $F_{\mu\nu}$ refers to three completely different gauge field tensors with their indices fully contracted...

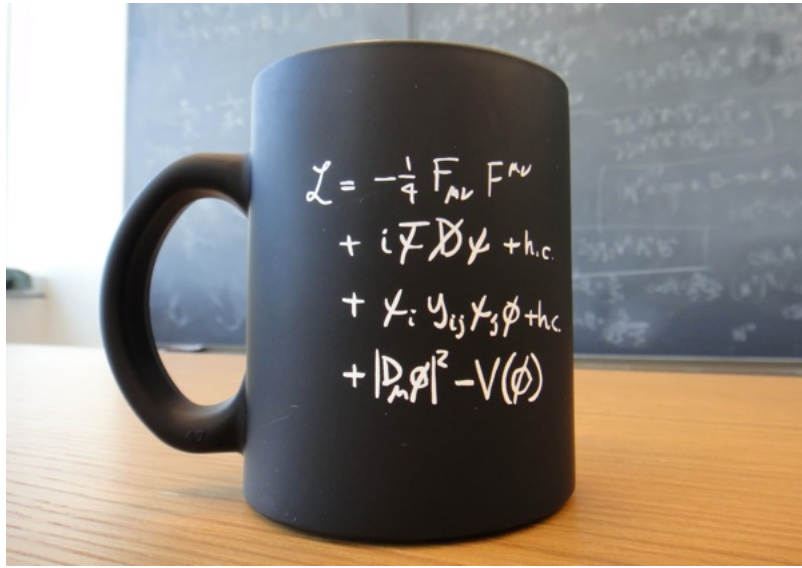


Figure 1.2: A coffee cup with the Standard Model Lagrangian density printed on its side. Please ignore the “+ h.c.” term following the $i\bar{\psi}D^\mu\psi$, it is the result of a small lapse in judgement from the mug makers.

3. The Strong Nuclear Force, which is responsible for holding quarks and gluons together in bound stands known as hadrons, like the protons and neutrons that make up everyday matter.

The only fundamental force missing from this list is the Gravitational Force, which is described by a completely separate set of equations²

Each of the three forces that are described within the Standard Model are mediated by different gauge bosons. For example, the electromagnetic force is mediated by the boson known as the photon, the weak nuclear force is mediated by the W and Z bosons, and the strong nuclear force is mediated by bosons known as gluons. In this thesis we will be primarily focusing on the Strong Nuclear Force, which acts solely on particles with color charge – an intrinsic property of quarks and gluons. The “color” charges are red, green, and blue with antio

Even though each of the electromagnetic, weak and strong forces can be described using the Standard Model Lagrangian, the way in which they appear within the

²Specifically, the Einstein Field Equations, $G_{\mu\nu} + \Lambda g_{\mu\nu} = \kappa T_{\mu\nu}$, but this is the thesis of a particle physicist so gravity is taboo.

equation is not easy to determine. For example, the electromagnetic force actually corresponds to line 1

Chapter Two: Experimental Apparatus

As this thesis is focused on the physics of heavy-ion collisions, it stands to reason that the data analyzed in this thesis was gathered using the only detector along the LHC dedicated to studying such collisions: the ALICE detector. In this chapter, a brief synopsis of the LHC will be provided, followed by a much more detailed overview of the ALICE detector and its corresponding sub-detectors.

2.1 The LHC

Located along the Swiss-French border near Geneva, Switzerland, the Large Hadron Collider (LHC) is the largest particle accelerator on the planet. At a circumference of 27 kilometers, its tunnels lie almost 200 meters beneath the surface of the earth. Inside the tunnels are two high-energy particle beams pointing in opposite directions, with the beam pipes being kept inside of an ultra-high vacuum. The particles inside the beam are guided by a multitude of superconducting magnets: 393 quadrupole magnets keep the beam focused, while 1232 dipole magnets bend the particles along the circular path. The beams are designed to collide at four intersection points along the LHC, each with a corresponding detector surrounding the collision points: (1) ALICE, which specializes in heavy-ion collisions; (2) ATLAS, which specializes in studying high- p_T particles produced in pp collisions, (3) CMS, which TODO and (4) LHCb, which is designed to study CP violations through measurements of B mesons at forward rapidity. A diagram of the LHC with these four intersection points can be seen in Figure 2.1.

Currently, the highest center of mass energies achieved for each of the main collision systems are $\sqrt{s} = 13$ TeV for pp, $\sqrt{s} = 7$ TeV for p-Pb and $\sqrt{s} = 5.02$ TeV for Pb-Pb. The LHC underwent a long shutdown from XXXX to YYYY, in order to upgrade the beam luminosity and COM energies. The projected final COM energies for each collision system will be ...

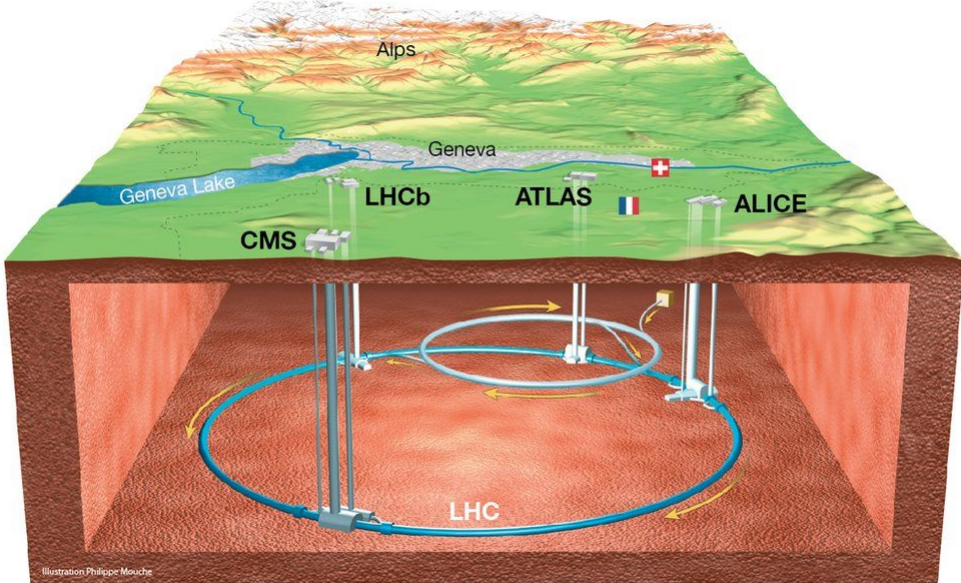


Figure 2.1: A diagram depicting the LHC with its various main detectors shown underground. Illustration by Phillippe Mouche, from BBC News.

2.2 The ALICE Detector

The detector used by the ALICE collaboration, unsurprisingly known as the ALICE detector, has the primary focus of investigating the physical properties of the strongly interacting quark-gluon plasma created during heavy-ion collisions. Building the detector was a massive effort, requiring the help from over 1000 people from 105 institutes in 30 different countries. The detector itself is also massive, weighing in at around 10,000 tons and spanning 26 meters in length with a 16-meter height and width. It is composed of 18 sub-detector systems, all of which work together to help reconstruct the event. A diagram of the detector with its corresponding sub-detector systems can be seen in Figure 2.2. As the primary focus of the ALICE detector is to study heavy-ion collisions, all of its components must work together to reconstruct very high multiplicity events.

2.2.1 The Inner Tracking System

The Inner Tracking System (ITS) is the inner-most component of the ALICE detector, lying closest to the beam pipe. It is composed of six cylindrical layers of silicon

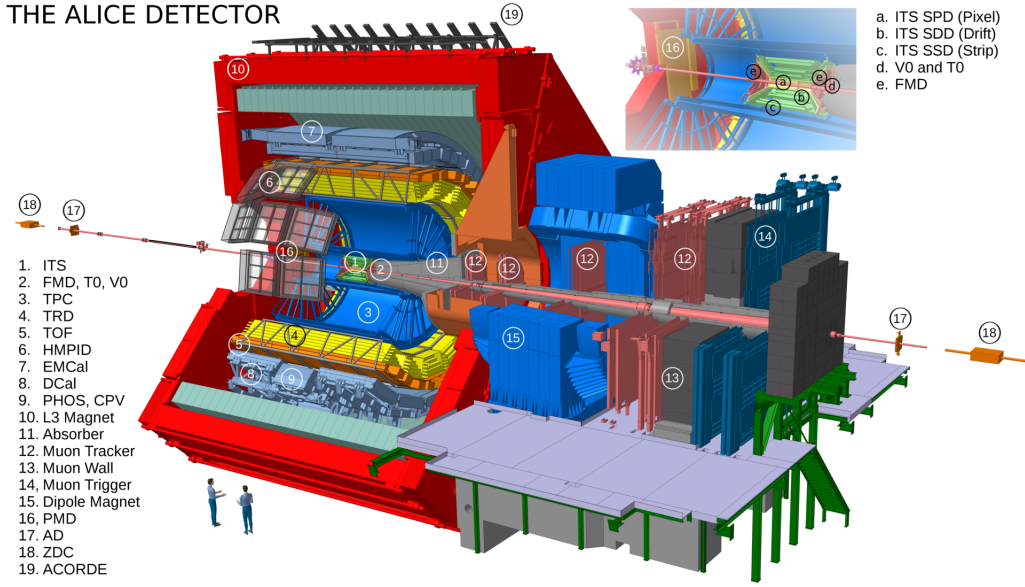


Figure 2.2: A 3-D schematic of the ALICE detector, with labels for all of the sub-detectors. Note the humans-for-scale in the bottom left of the diagram.

detectors that are coaxial with the beam pipe and cover the pseudorapidity range $|\eta| \leq 0.9$. The distance from the beam line varies from 3.9 cm for the first layer to 43 cm for the sixth layer. The ITS uses different types of silicon detectors for each layer: Silicon Pixel Detectors (SPD) for the first and second layers, Silicon Drift Detectors (SDD) for the third and fourth layers, and double sided Silicon Strip Detectors (SSD) for the fifth and sixth layers. Because of its proximity to the interaction point, the ITS is invaluable for reconstructing both primary and secondary vertices and enhancing the tracking capabilities of the ALICE detector near the interaction point. Moreover, the ITS can also track particles that are not detected or missed by the external barrel detector due to acceptance limitations and momentum cutoff.

2.2.1.1 ITS Upgrade

The LHC underwent a fairly substantial upgrade to the beam luminosity from X to Y. In order to utilize all of the The writer of this thesis was the main reason why the ITS Upgrade actually finished, as he is the smartest person of all time and actually hand built the entire thing.

2.2.2 The V0 Detector

V0 is made of two arrays of scintillator counters set on both sides of the ALICE interaction point, and called V0-A and V0-C. The V0-C counter is located upstream of the dimuon arm absorber and cover the spectrometer acceptance while the V0-A counter will be located at around 3.5 m away from the collision vertex, on the other side. It is used to estimate the centrality of the collision by summing up the energy deposited in the two disks of V0. This observable scales directly with the number of primary particles generated in the collision and therefore to the centrality. V0 is also used as reference in Van Der Meer scans that give the size and shape of colliding beams and therefore the luminosity delivered to the experiment.

2.2.3 The Time Projection Chamber

The largest component of the ALICE detector is known as the Time Projection Chamber (TPC). The TPC is a gas-filled volume with The ALICE Time Projection Chamber (TPC) is a large volume filled with a gas as detection medium and is the main particle tracking device in ALICE.[19][20] Charged particles crossing the gas of the TPC ionize the gas atoms along their path, liberating electrons that drift towards the end plates of the detector. The characteristics of the ionization process caused by fast charged particles passing through a medium can be used for particle identification. The velocity dependence of the ionization strength is connected to the well-known Bethe-Bloch formula, which describes the average energy loss of charged particles through inelastic Coulomb collisions with the atomic electrons of the medium. Multiwire proportional counters or solid-state counters are often used as detection medium, because they provide signals with pulse heights proportional to the ionization strength. An avalanche effect in the vicinity of the anode wires strung in the readout chambers, gives the necessary signal amplification. The positive ions created in the avalanche induce a positive current signal on the pad plane. The readout is performed by the 557 568 pads that form the cathode plane of the multi-wire proportional chambers (MWPC) located at the end plates. This gives the radial distance to the beam and the azimuth. The last coordinate, z along the beam direction, is given by the drift time. Since energy-loss fluctuations can be considerable, in general many pulse-height measurements are performed along the particle track in order to optimize the resolution of the ionization measurement. Almost all

of the TPC’s volume is sensitive to the traversing charged particles, but it features a minimum material budget. The straightforward pattern recognition (continuous tracks) make TPCs the perfect choice for high-multiplicity environments, such as in heavy-ion collisions, where thousands of particles have to be tracked simultaneously. Inside the ALICE TPC, the ionization strength of all tracks is sampled up to 159 times, resulting in a resolution of the ionization measurement as good as 5

2.2.4 The Electromagnetic Calorimeter

The EMCAL is a lead-scintillator sampling calorimeter comprising almost 13,000 individual towers that are grouped into ten super-modules. The towers are read out by wavelength-shifting optical fibers in a shashlik geometry coupled to an avalanche photodiode. The complete EMCAL will contain 100,000 individual scintillator tiles and 185 kilometers of optical fiber, weighing in total about 100 tons. The EMCAL covers almost the full length of the ALICE Time Projection Chamber and central detector, and a third of its azimuth placed back-to-back with the ALICE Photon Spectrometer – a smaller, highly granular lead-tungstate calorimeter. The super-modules are inserted into an independent support frame situated within the ALICE magnet, between the time-of-flight counters and the magnet coil. The support frame itself is a complex structure: it weighs 20 tons and must support five times its own weight, with a maximum deflection between being empty and being fully loaded of only a couple of centimeters. Installation of the eight-ton super-modules requires a system of rails with a sophisticated insertion device to bridge across to the support structure. The Electro-Magnetic Calorimeter (EM-Cal) will add greatly to the high momentum particle measurement capabilities of ALICE.[26] It will extend ALICE’s reach to study jets and other hard processes.

Chapter Three: Analysis Details

This chapter builds upon the analysis overview presented in the previous chapter by providing a much more detailed description of each component of the analysis. These components can be summarized as follows. First, a high-quality data sample of p–Pb collisions is selected, with events further differentiated by their multiplicity. Then, quality tracks are selected for the trigger and associated charged hadrons, and the Λ baryons are reconstructed from lower quality tracks using their characteristic decay topology. These Λ daughter tracks are identified as protons or pions using information from the TPC and TOF detectors. Within a given event, the trigger hadrons are then combined with either the associated charged hadrons or the Λ candidates to form pairs, where a distribution of their relative azimuthal angle ($\Delta\varphi \equiv \varphi_{trig.} - \varphi_{assoc.}$) and pseudorapidity ($\Delta\eta \equiv \eta_{trig.} - \eta_{assoc.}$) is filled for each pair. These h– Λ and h–h angular distributions are then corrected for a laundry list of detector effects using both data- and MonteCaro-driven methods. Further corrections are applied to the h– Λ distributions to account for effects like the combinatorial background associated with the Λ reconstruction and the two-track merging effect, whereby one of the daughter tracks gets merged with the trigger hadron track, causing a h– Λ pair deficit at small angles. Once all corrections are applied, the h– Λ and h–h distributions are finalized and ready for the extracting of the many observables discussed at the end of the previous chapter.

3.1 Dataset and event selection

3.1.1 Dataset

Every event in this analysis was a p–Pb collision at $\sqrt{s_{NN}} = 5.02$ TeV with data collected by the ALICE detector during the 2016 LHC run. This analysis uses the data from these runs with the “FAST” reconstruction, meaning the data was taken without the ITS’s SDD subdetector due to issues with readout during this period. The total number of events (prior to any selection) is roughly 400 million. For the efficiency studies, the analysis was performed using a standard purpose MC-generated

production anchored to the dataset using the DPMJET [9] event generator. This production consists of around 400 million minimum bias events, which is roughly equivalent to data.

3.1.2 Event Selection

Events are selected by requiring the location of the primary collision interaction point (called the “primary vertex” or PV) to be no more than 10 cm from the center of the detector along the beam axis or “z”-direction. Furthermore, every event is required to have at least three reconstructed tracks that contributed to the reconstruction of the PV. This reduces the total number of events considered to approximately 350 million events, and a summary of the effects of these selection criteria can be seen in Table 3.1. The events are further separated into three charged particle multiplicity classes (0-20%, 20-50% and 50-80%) based off event activity in the forward-rapidity V0A detector.

Table 3.1: Number of events passing our criteria for each multiplicity bin considered. Here Z_{vtx} refers to the position of the PV along the beam (z) axis.

Multiplicity	Total evts.	Has 3 tracks	$ Z_{vtx} < 10\text{cm} + 3 \text{ tracks}$	% Pass
0-20%	1.0E08	1.0E08	0.8E08	87%
20-50%	1.6E08	1.6E08	1.3E08	86%
50-80%	1.6E08	1.6E08	1.3E08	86%

3.2 Charged hadron track selection

3.2.1 Trigger track cuts

For any two-particle correlation analysis, the selection criteria of the trigger hadron is of utmost importance as any geometric biases introduced by the trigger selection could be reflected in the final correlation distributions. However, correlation analyses generally require large statistics, thus the selection criteria shown in Table 3.2 are applied to ensure the quality of the trigger hadron track while maximizing the statistics of the analysis. Furthermore, the trigger hadron tracks are required to be

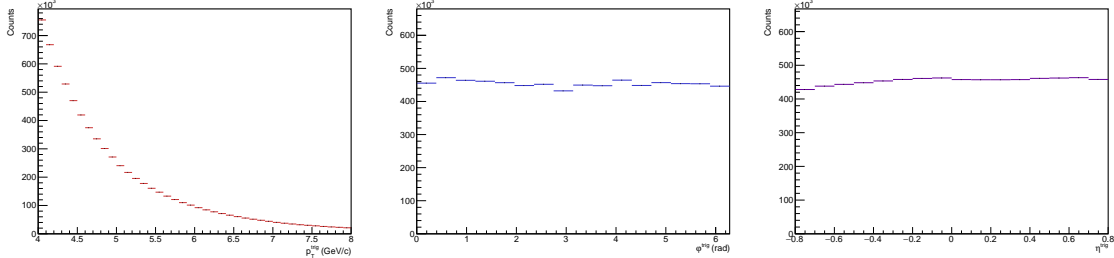


Figure 3.1: The p_T (left), φ (middle) and η (right) distributions for the trigger hadrons in the multiplicity range 0-20%.

at midrapidity ($|\eta| < 0.8$) and have high¹ momentum with $4.0 < p_T^{\text{trig.}} < 8.0 \text{ GeV}/c$, as the trigger is meant to serve as a proxy for a jet axis. Plots of the p_T , φ and η distributions for the trigger hadrons that pass these cuts in the 0-20% multiplicity bin can be seen in Figure 3.1.

Table 3.2: The track quality cuts applied to the trigger hadrons in this analysis.

Selection criterion	Value
TPC clusters	≥ 50
χ^2 per TPC cluster	< 4
Fraction of shared TPC clusters	< 0.4
DCA _{xy}	< 2.4 cm
DCA _z	< 3.2 cm
Accept kink daughters	No

3.2.2 Associated hadron track cuts

To keep the results of this analysis more comparable to previous measurements of the $\Lambda/\pi \approx \Lambda/h$ ratio, the selection criteria for the associated hadrons are more strict than those for the trigger hadrons as the associated hadrons are meant to be “primary”, meaning they did not originate from a weak decay. All associated hadrons are required to meet the ALICE standard track quality cuts for primary charged hadrons described in Table 3.3. Furthermore, the associated hadrons are selected only at midrapidity ($|\eta| < 0.8$) in the momentum region $1.0 < p_T < 4.0 \text{ GeV}/c$, with further binning

¹“High” in this case means high enough to guarantee the hadron is produced close (in $\Delta\varphi\Delta\eta$ -space) to a jet axis.

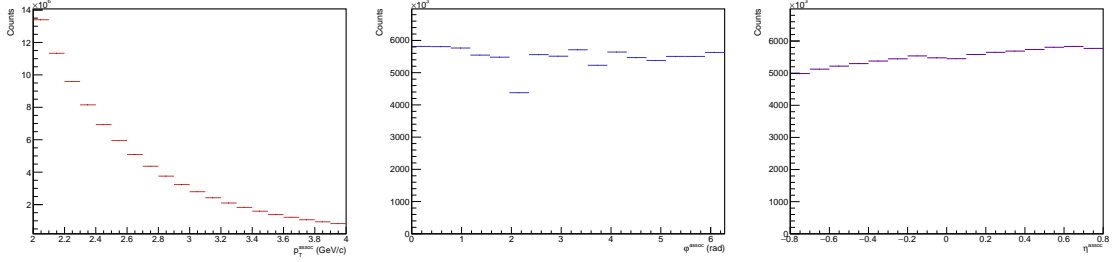


Figure 3.2: The p_T (left), φ (middle) and η (right) distributions for the associated hadrons in the multiplicity range 0-20%. The dips observed in the φ distribution are due to the TPC sector boundaries.

performed offline. The p_T , φ and η distributions for the associated hadrons that pass these cuts in the 0-20% multiplicity bin can be seen in Figure 3.2.

Table 3.3: The ALICE standard track quality cuts for primary charged hadrons, used for the selection of the associated hadrons in this analysis.

Selection criterion	Value
Crossed rows in TPC	≥ 80
Crossed rows/findable clusters in TPC	> 0.8
TPC clusters	≥ 80
ITS clusters	≥ 3
χ^2 per TPC cluster	< 4
χ^2 per ITS cluster	< 36
TPC and ITS refit required	Yes
DCA _{xy}	$< 0.0105 + 0.0350/p_T^{1.1}$ cm
DCA _z	< 2 cm

3.3 Λ reconstruction

3.3.1 Characteristic V⁰ decay topology

The Λ candidates in this analysis are reconstructed using their characteristic “V”-shaped decay topology, which is seen in the detector as two oppositely charged tracks originating from a common vertex which is sufficiently displaced from the PV (called the “secondary vertex” or SV). Such particles capable of being reconstructed via this topology are called “V⁰’s: the V describing the decay shape and the 0 indicating that

the particle is neutral. A diagram depicting a typical V^0 decay is shown in Figure 3.3, with labels given for the most relevant kinematic variables.

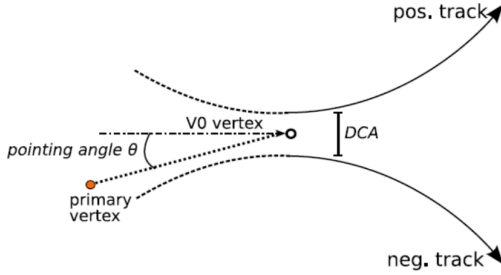


Figure 3.3: A diagram depicting a typical V^0 decay with labels for the most important kinematic variables. The diagram was taken from [10].

The first and most important of these variables is the distance of closest approach (DCA) between the two tracks. This DCA needs to be small enough (relative to the tracking resolution) to ensure that the tracks originated from a common vertex. Another important variable is the transverse decay length of the V^0 , which is the distance between the PV and the SV measured in the xy -plane. The importance of this variable is twofold: if the decay length is too small, then it may not even be possible to resolve the SV from the PV, plus it allows for the distinction between V^0 s of differing decay lengths. The final relevant variable is the cosine of the pointing angle, which is the angle between the momentum vector of the V^0 and the vector pointing from the PV to the SV. As V^0 candidates are generally required to be sufficiently collimated to ensure that the V^0 originated from the PV, the cosine of the pointing angle is usually close to unity.

Using these variables, a list of likely V^0 candidates is generated for each event, from which further cuts are applied to maximize the likelihood of the candidate being a true Λ baryon. These cuts are summarized in the following section. There is also another technique for Λ reconstruction whereby all oppositely charged proton-pion pairs are combined to form Λ candidates, which is explored in more detail in Chapter 4. However, due to the large combinatorial background associated with this technique, the V^0 method described above is nominal for this analysis.

3.3.2 Λ daughter proton and pion track cuts

Because of the longer decay length of the Λ ($c\tau \approx 10$ cm), the corresponding daughter proton and pion tracks generally have fewer hits in both the ITS and TPC, resulting in “lower quality” track parameters. Because of this, the cuts applied to the daughter tracks used to reconstruct Λ candidates are the least strict of all the track quality cuts in this analysis and are summarized in Table 3.4. The daughter proton and pion are also required to be at midrapidity ($|\eta| < 0.8$) and have a minimum p_T of $p_T > 0.15$ GeV/ c .

Table 3.4: The track quality cuts applied to both the daughter proton and pion tracks used to reconstruct Λ candidates. These cuts are intentionally less strict than those applied to the trigger and associated hadrons as the daughter tracks are reconstructed from secondary particles.

Selection criterion	Value
TPC refit required	Yes
Crossed rows in TPC	≥ 70
Crossed rows/findable clusters in TPC	> 0.8

Following the particle identification procedure outlined in Sections ?? and ??, the daughter proton and pion tracks are required to pass the following PID cuts using both the TPC and TOF detectors:

- $|n\sigma_{\text{TPC},p}| < 2$
- $|n\sigma_{\text{TPC},\pi}| < 3$
- $|n\sigma_{\text{TOF},p}| < 2$ (if signal exists)
- $|n\sigma_{\text{TOF},\pi}| < 3$ (if signal exists)

The values of these cuts were chosen to maximize the Λ signal while avoiding contamination from other particle species. The parenthetical “if signal exists” means that the TOF PID cut is only applied if the track has a TOF signal. Due to the large distance between the TOF detector and the PV, many lower momentum tracks are deflected by the magnetic field before reaching the TOF detector, resulting in no signal. Excluding such tracks results in a more pure sample of protons and pions, at the cost of a much lower number of Λ candidates. While such a cost is not

acceptable for the nominal analysis, the effect of excluding these tracks is investigated in Chapter 4. The $n\sigma$ distributions for both the TPC and TOF detectors of the daughter proton and pion tracks that pass the aforementioned quality cuts are shown in Figure 3.4 and Figure 3.5, respectively. To check for contamination from other particle species, the TOF and TPC information is combined to form a $n\sigma_{\text{TOF}}$ vs $n\sigma_{\text{TPC}}$ plot, which is shown for both the protons and pions in Figure 3.6. No contamination is observed for either the proton or pion tracks.

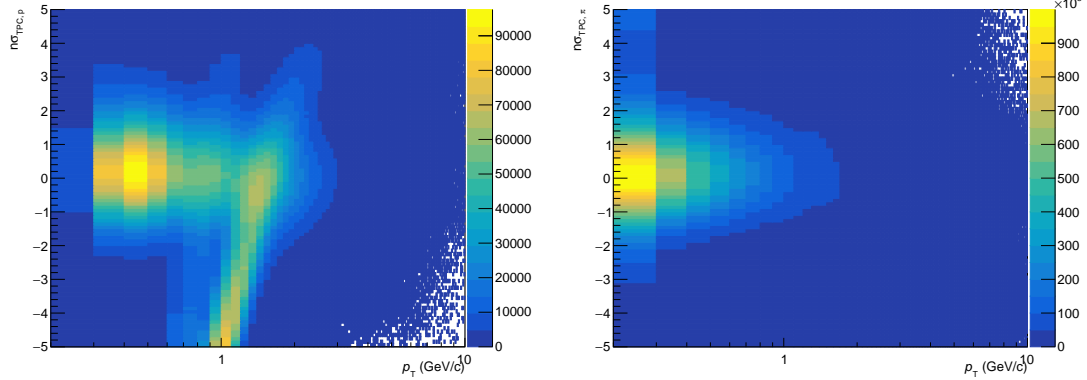


Figure 3.4: $n\sigma$ for protons (left) and pions (right) in the TPC detector as a function of p_T .

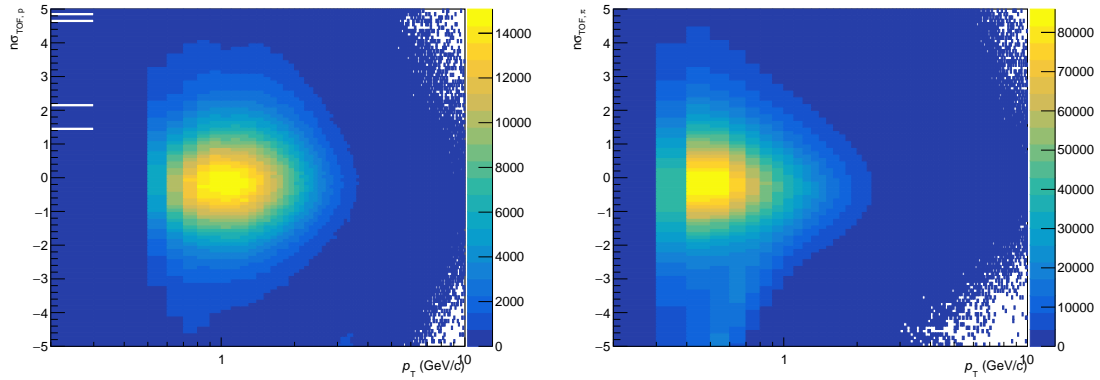


Figure 3.5: $n\sigma$ for protons (left) and pions (right) in the TOF detector as a function of p_T .

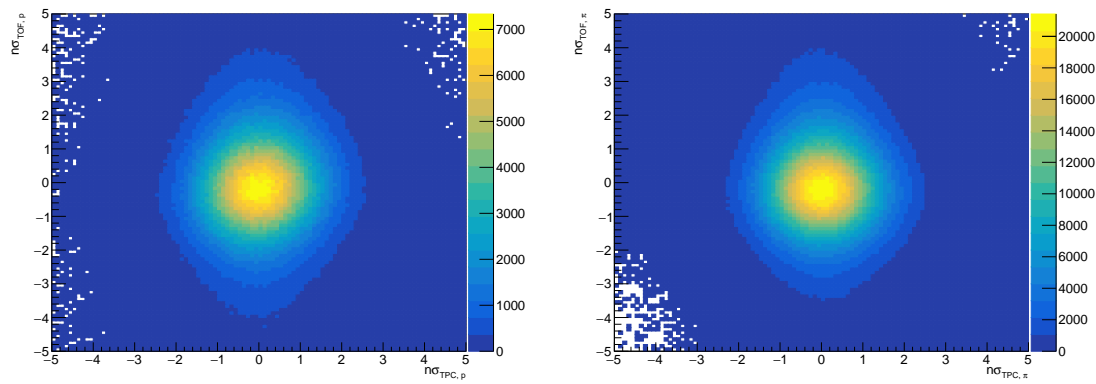


Figure 3.6: $n\sigma$ in TOF vs $n\sigma$ in TPC for protons (left) and pions (right). No contamination is observed for both of the particle species.

3.3.3 Λ candidate selection

With the daughter proton and pion tracks selected, the Λ candidates are generated by combining all oppositely charged proton-pion pairs into V^0 s which meet the topological selection criteria described in Table 3.5.

Table 3.5: Topological selection criteria applied to Λ candidates.

Selection criterion	Value
$ \eta $	< 0.8
Decay radius (cm)	> 0.2
DCA _{xy} of pion track to PV (cm)	> 0.06
DCA _{xy} of proton track to PV (cm)	> 0.06
DCA _{xy} between daughter tracks ($n\sigma$)	< 1.5
$\cos(\theta_{\text{pointing}})$	> 0.9
Invariant mass (GeV/c^2)	$1.102 < M_{p\pi} < 1.130$

The invariant mass $M_{p\pi}$ is calculated using

$$M_{p\pi} = \sqrt{(E_p + E_\pi)^2 - (\vec{p}_p + \vec{p}_\pi)^2}, \quad (3.1)$$

where $E_x = \sqrt{m_x^2 + p_x^2}$ is the energy of the particle of species x . The $M_{p\pi}$ distributions for the Λ candidates for all multiplicity and momentum bins are shown in Figure 3.7. The distributions are also fit with a Voigtian function (convolution of Breit-Wigner and Gaussian [11]) plus a straight line to describe the background. Note that despite our selection criteria, there is still a non-negligible background due to the presence of misidentified Λ candidates. As this background inevitably makes its way into the final h- Λ correlation distributions, it is removed using the technique described in Section ??.

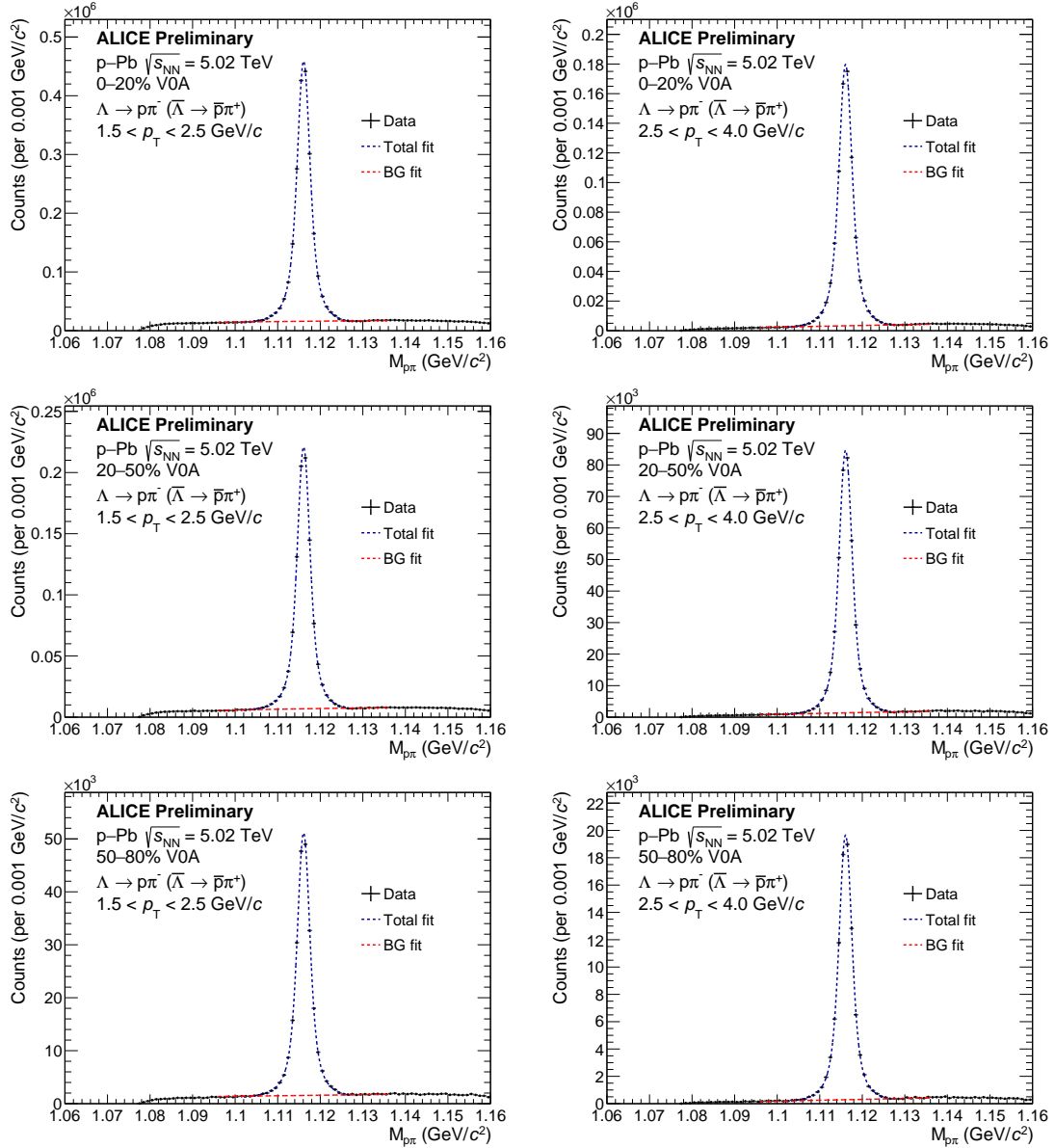


Figure 3.7: Invariant mass distributions in the 0-20% (top), 20-50% (middle), and 50-80% (bottom) multiplicity bins for the Λ candidates which pass the selection criteria with $1.5 < p_T < 2.5 \text{ GeV}/c$ (left) and $2.5 < p_T < 4.0 \text{ GeV}/c$ (right). A Voigtian signal + straight-line background fit to the data is shown in blue, with just the background fit shown in red. For these plots, the Λ s were only reconstructed in events with a trigger hadron.

3.4 Reconstruction efficiency

In an ideal world, the number of reconstructed particles of interest would be equal to the number of particles produced in the collision. Unfortunately this is not the case, as there are a number of detector effects which can cause particles to be “lost” during reconstruction. To correct for these effects, the reconstruction efficiency

$$\epsilon(x_1, x_2, \dots, x_n) \equiv P(f(x_1, x_2, \dots, x_n) | g(x_1, x_2, \dots, x_n)), \quad (3.2)$$

is used. Here x_i are the kinematic variables of the particle of interest (e.g. p_T , η , φ), $f(x_1, x_2, \dots, x_n)$ is the probability that a particle is reconstructed (“found”) with kinematic variables x_i , and $g(x_1, x_2, \dots, x_n)$ is the probability that a particle is produced (“generated”) with the same variables. While the distributions f and g are inaccessible within a given event, the efficiency can be calculated using Monte Carlo simulation techniques via the equation

$$\epsilon(x_1, x_2, \dots, x_n) = \frac{N_{\text{reco.}}(x_1, x_2, \dots, x_n)}{N_{\text{gen.}}(x_1, x_2, \dots, x_n)}, \quad (3.3)$$

where $N_{\text{reco.}}$ and $N_{\text{gen.}}$ are the reconstructed and generated particle distributions, respectively, usually taken across a large number of simulated events. In this analysis, these distributions are calculated as a function of p_T and η for each multiplicity class using 30 million events generated by the Monte Carlo event generator DPM-JET [9] with particle propagation through the ALICE detector performed by the GEANT3 [12] detector simulation software. These efficiency distributions are then used to correct the h- Λ and h-h correlation distributions using the procedure described in Section 3.5.

3.4.1 Charged hadron reconstruction efficiency

The trigger and associated hadron track reconstruction efficiencies are calculated using Equation 3.3, where the trigger and associated hadrons from $N_{\text{reco.}}$ are subject to the following:

- The track passes the quality cuts outlined in Tables 3.2 (trigger) or 3.3 (associated)
- The track has a corresponding generated particle

- That generated particle is either a pion, proton, kaon, electron or muon
- $|\eta_{\text{track}}| \leq 0.8$,

and the trigger and associated hadrons from N_{gen} . are subject to:

- $|\eta_{\text{track}}| \leq 0.8$
- The particle is either a pion, proton, kaon, electron or muon
- The particle is primary (i.e. did not originate from a weak decay)

The trigger and associated track reconstruction efficiencies are shown for each multiplicity class as a function of p_T in Figure 3.8. While these efficiencies exhibit relatively flat behavior as a function of p_T and multiplicity, they are still treated as p_T and multiplicity dependent during the correction procedure.

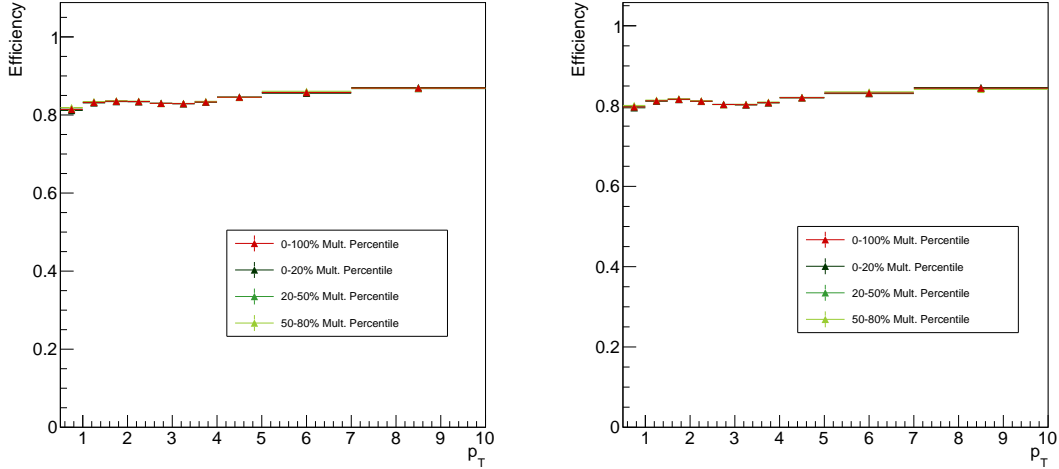


Figure 3.8: Efficiency vs. p_T for trigger (left) and associated (right) hadrons. While they may look identical, the associated hadron efficiency is slightly lower due to the stricter selection criteria.

3.4.2 Λ reconstruction efficiency

The Λ reconstruction efficiency is calculated as a function of p_T and η using Equation 3.3, where the Λ s from N_{reco} . are subject to the following:

- They pass the topological selection criteria from Table 3.5
- The reconstructed daughter p, π tracks pass the quality cuts from Table 3.4
- The daughter p, π tracks have corresponding generated p, π particles
- Those generated p, π daughters come from the same mother Λ
- $|\eta_\Lambda| \leq 0.8$,

and the Λ s from $N_{\text{gen.}}$ are subject to:

- $|\eta_\Lambda| \leq 0.8$
- The Λ decays to $p\pi$.

The requirement that the generated Λ s decay into $p\pi$ means the branching ratio is not included in the efficiency calculation as it is corrected for separately (see Section 3.5). The Λ reconstruction efficiency can be seen for each multiplicity class as a function of p_T and η in Figure 3.9. Note that the efficiency is no longer flat as a function of η due to the $|\eta| < 0.8$ requirement for the daughter tracks, which kinematically restricts the Λ reconstruction to a smaller η range.

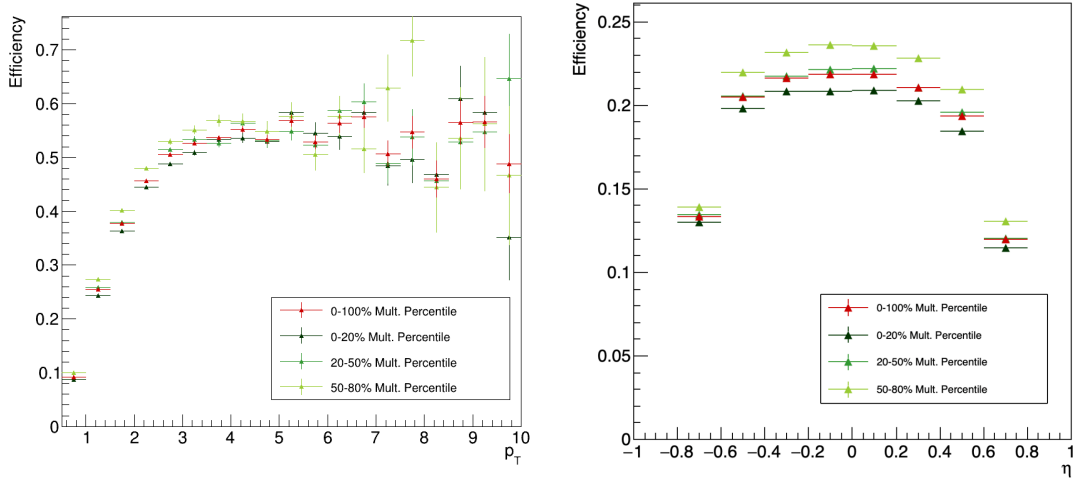


Figure 3.9: Efficiency vs. p_T (left) and η (right) for Λ reconstruction in each multiplicity bin, along with an integrated 0-100% point in red.

3.5 Corrections to the correlation distributions

Once the trigger and associated particles are selected, the two-particle h- Λ and h-h correlation distributions are generated. As mentioned in the previous chapter, the corrected two-particle correlation function is given by

$$\frac{1}{N_{trig}} \frac{d^2 N_{pair}}{d\Delta\varphi d\Delta\eta} = \frac{1}{N_{trig}^{corr}} \frac{1}{\epsilon_{trig} \times \epsilon_{assoc}} B(0, 0) \frac{S(\Delta\varphi, \Delta\eta)}{B(\Delta\varphi, \Delta\eta)}. \quad (3.4)$$

which contains a number of explicit correction terms (in the form of ϵ s) along with some implicit corrections. These corrections are described in this section, and are presented in the order in which they are applied to the data.

3.5.1 Single-particle efficiency corrections

As both the trigger and the associated particles have their own independent reconstruction efficiencies, the trigger-associated pair reconstruction efficiency should be

$$\epsilon_{trig,assoc} = \epsilon_{trig} \times \epsilon_{assoc}, \quad (3.5)$$

meaning the single-particle efficiency distributions from Section 3.4 can be used to calculate the weight $1/(\epsilon_{trig} \times \epsilon_{assoc})$. This weight is applied for each h- Λ and h-h pair in the two-dimensional correlation distribution. However, the assumption that the reconstruction efficiencies are independent is slightly incorrect in the case of the h- Λ distributions due to track merging effects, thus an additional ϵ_{pair} correction is required (discussed in detail in Section 3.5.3).

The trigger efficiency weight $1/\epsilon_{trig}$ is also applied to the single-particle trigger hadron distribution in data to obtain N_{trig}^{corr} .

3.5.2 Mixed-event acceptance correction

As mentioned in Section ??, the $B(0, 0)/B(\Delta\varphi, \Delta\eta)$ term in Equation 3.4 corrects for the finite acceptance along η as both our trigger and associated particles are required to be within $|\eta| < 0.8$. The mixed-event distribution $B(\Delta\varphi, \Delta\eta)$ shown in Figure ?? has a characteristic triangular shape along $\Delta\eta$, which is purely due to detector geometry as no physical correlations are present. When scaled by $1/B(0, 0)$, the mixed event distribution becomes the probability that a particle pair is found given

that the trigger particle is within $|\eta| < 0.8$, which is unity at $\Delta\varphi, \Delta\eta = 0, 0$. Thus correcting the same-event distribution $S(\Delta\varphi, \Delta\eta)$ by $B(0, 0)/B(\Delta\varphi, \Delta\eta)$ removes this acceptance effect and allows for a more accurate determination of the pair-wise yields.

While the generation of the mixed event distribution $B(\Delta\varphi, \Delta\eta)$ was discussed briefly in Section ??, the specific details are as follows. First, in order to ensure that the mixed-event pairs are coming from similar events, the events in the mixing pool are separated by both multiplicity percentile and Z_{vtx} position. The categorizing of events based off of Z_{vtx} position is an integral part of the acceptance correction: events with a Z_{vtx} at one edge of the detector have a completely different (and nearly inverted) η acceptance than those on the opposite edge. The multiplicity bins are the same as they are for the same-event distributions (namely 0-20%, 20-50% and 50-80%), and the ten Z_{vtx} bins are split evenly from -10 cm to 10 cm. For each multiplicity and Z_{vtx} bin, the acceptance correction

$$S_{\text{corr.}}(\Delta\varphi, \Delta\eta) = \frac{S(\Delta\varphi, \Delta\eta)}{B(\Delta\varphi, \Delta\eta)/B(0, 0)} \quad (3.6)$$

is performed, and the results for each multiplicity bin are then merged across all Z_{vtx} bins. The same-event distributions are also split into Z_{vtx} bins during this correction procedure. The uncorrected distributions $S(\Delta\varphi, \Delta\eta)$ and the mixed-event distributions $B(\Delta\varphi, \Delta\eta)$ are shown for both the h- Λ and h-h cases for all multiplicity and associated momentum bins in Figures 3.10 through 3.13.

This mixed-event correction is the final correction applied to the h-h distributions. However, the h- Λ distributions require additional corrections that are not present in the dihadron case.

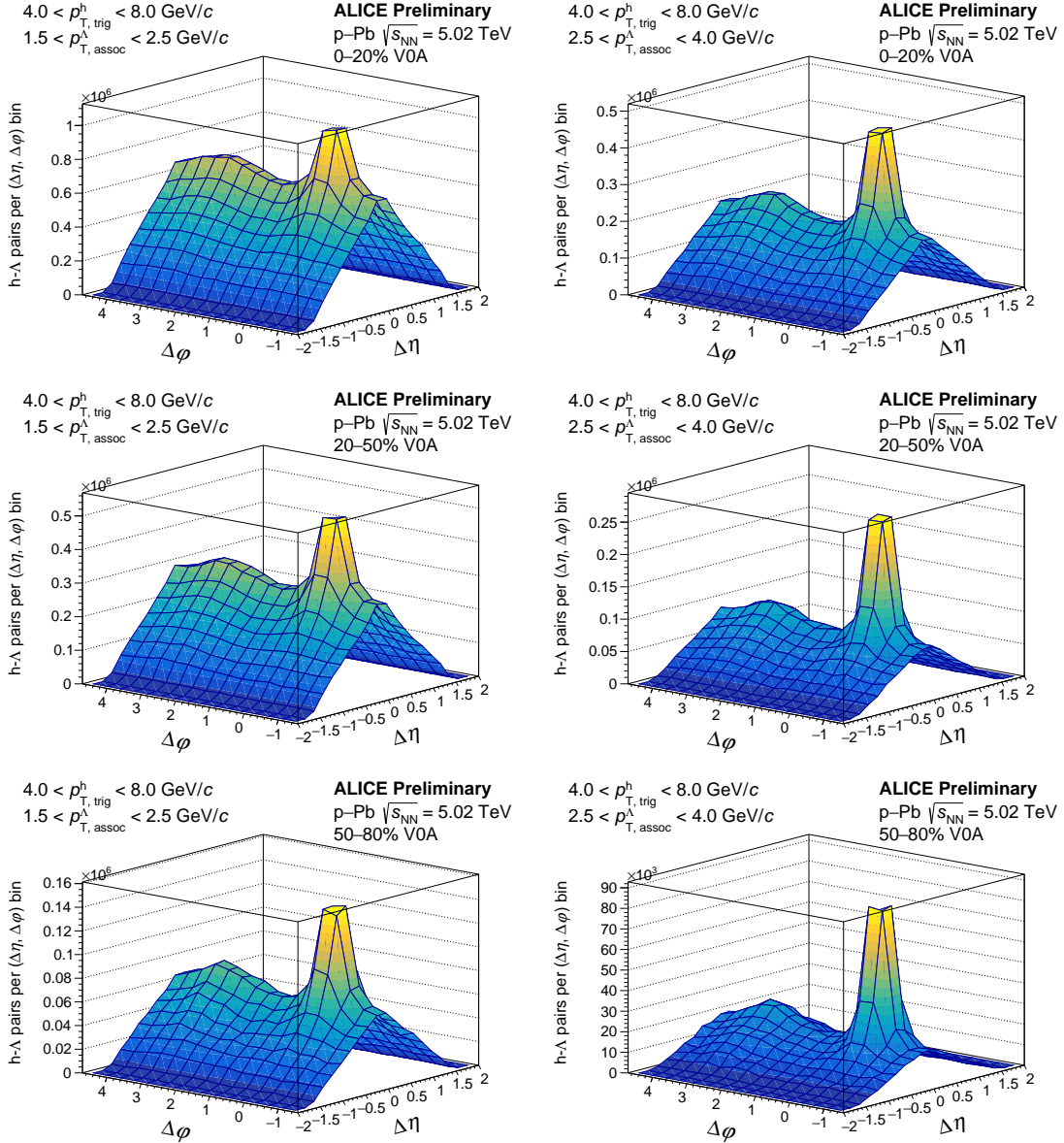


Figure 3.10: 2-D non-acceptance corrected $h\bar{\Lambda}$ angular correlations for the 0–20% (top), 20–50% (middle), and 50–80% (bottom) multiplicity bins for $1.5 < p_T < 2.5 \text{ GeV}/c$ (left) and $2.5 < p_T < 4.0 \text{ GeV}/c$ (right).

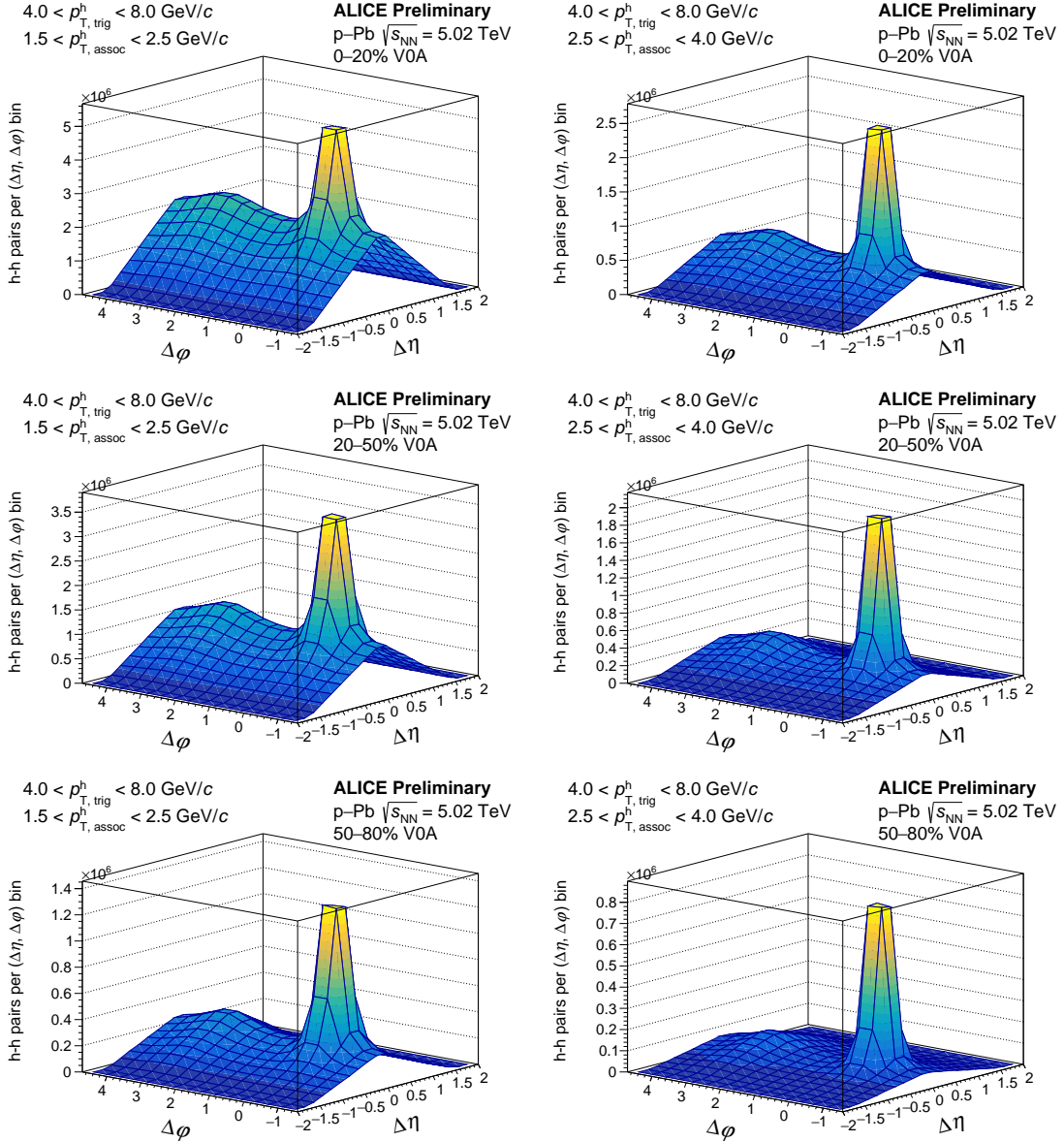


Figure 3.11: 2-D non-acceptance corrected h-h angular correlations for the 0-20% (top), 20-50% (middle), and 50-80% (bottom) multiplicity bins for $1.5 < p_T < 2.5 \text{ GeV}/c$ (left) and $2.5 < p_T < 4.0 \text{ GeV}/c$ (right).

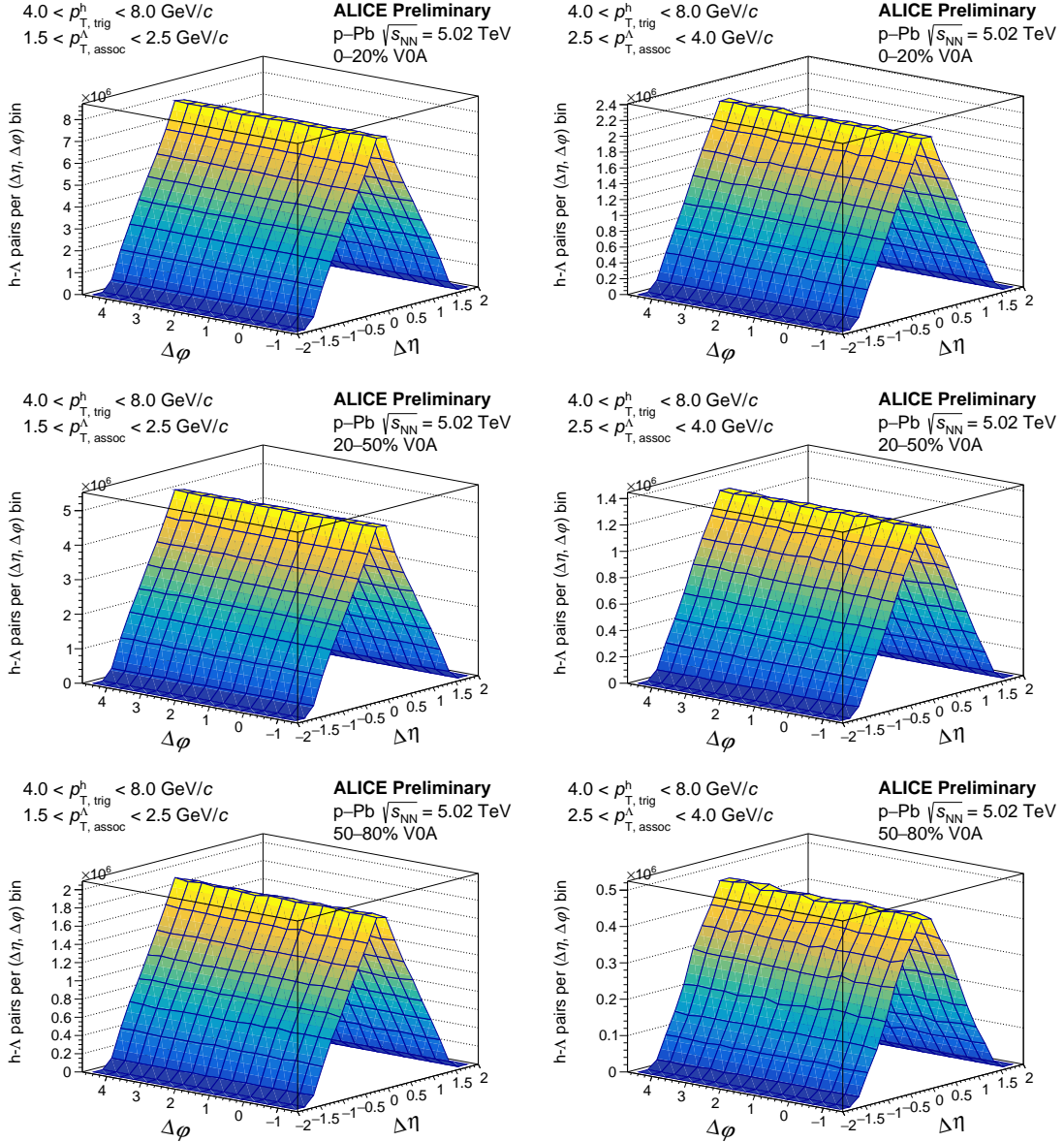


Figure 3.12: 2-D mixed-event $h\bar{\Lambda}$ angular correlations for the 0-20% (top), 20-50% (middle), and 50-80% (bottom) multiplicity bins for $1.5 < p_T < 2.5 \text{ GeV}/c$ (left) and $2.5 < p_T < 4.0 \text{ GeV}/c$ (right). The Z_{vtx} bins are merged together for these plots.

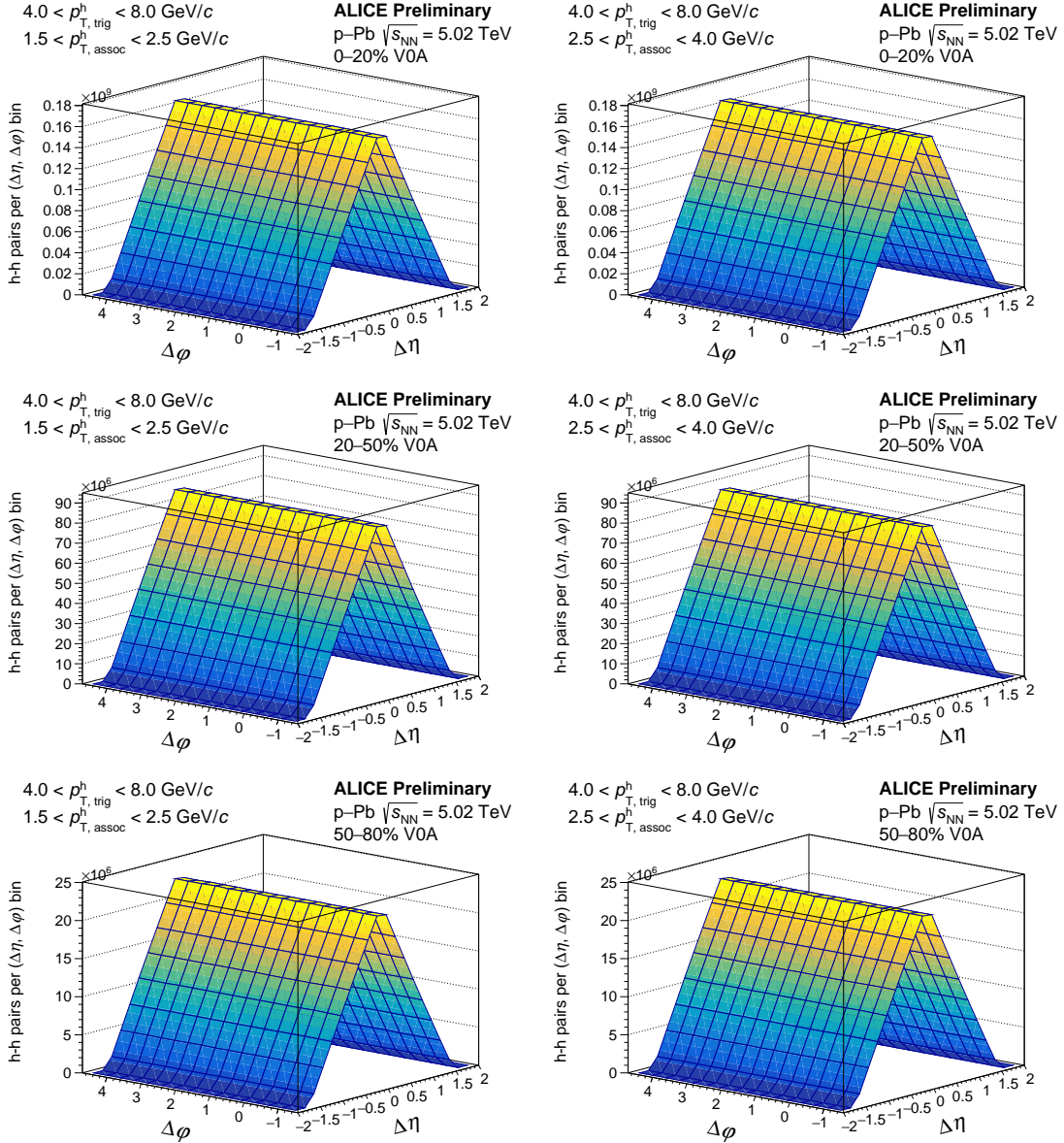


Figure 3.13: 2-D mixed-event h-h angular correlations for the 0-20% (top), 20-50% (middle), and 50-80% (bottom) multiplicity bins for $1.5 < p_T < 2.5$ GeV/c (left) and $2.5 < p_T < 4.0$ GeV/c (right). The Z_{vtx} bins are merged together for these plots.

3.5.3 Additional corrections for the h- Λ distributions

While the corrected correlation function from Equation 3.4 is generally true for two-particle correlations, there are a few additional corrections that must be applied to the h- Λ distributions due to the Λ reconstruction procedure and the presence of track merging effects. To formalize this, the corrected h- Λ correlation function can be written as

$$C_{\text{corr.}}^{\text{h-}\Lambda}(\Delta\varphi, \Delta\eta) = \frac{r_{\text{signal}} \times r_{\text{branch}}}{\epsilon_{\text{pair}}(\Delta\varphi, \Delta\eta)} \left(C_{\text{signal}}^{\text{h-p}\pi}(\Delta\varphi, \Delta\eta) - r_{\text{comb.}} \times C_{\text{sideband}}^{\text{h-p}\pi}(\Delta\varphi, \Delta\eta) \right), \quad (3.7)$$

where $C_{\text{corr.}}^{\text{h-}\Lambda}$ is the final corrected h- Λ distribution. Each term on the RHS of the equation will be described in detail in the following sections, and they are presented in the order in which they are applied to the distributions.

3.5.3.1 Combinatorial background removal

The term

$$C_{\text{signal}}^{\text{h-p}\pi}(\Delta\varphi, \Delta\eta) - r_{\text{comb.}} \times C_{\text{SB, norm.}}^{\text{h-p}\pi}(\Delta\varphi, \Delta\eta) \quad (3.8)$$

describes the removal of the combinatorial background resulting from the Λ reconstruction procedure from Section 3.3 using the **sideband subtraction** technique. The $C_{\text{signal}}^{\text{h-p}\pi}$ distribution corresponds to Λ candidates where the invariant mass of the p π pair falls within the range specified in Table 3.5, and the self-normalized $C_{\text{SB, norm.}}^{\text{h-p}\pi}$ distribution corresponds to candidates where the mass of the p π pair falls within the so-called “sideband” region. An invariant mass plot highlighting these different regions can be seen in Figure 3.14. Both of the C_{signal} and C_{sideband} distributions are corrected for acceptance and efficiency using the techniques described in the previous sections. The sideband region is chosen such that it is far enough away from the signal region to be free of any Λ signal, but close enough to ensure that the background p π pairs in the signal region are kinematically similar to the pairs in the sideband region as to not introduce any biases in the correlations. The underlying assumption of this technique is that the correlation shape of h-p π pairs from the sideband region is the same as the shape from the background h-p π pairs in the signal region. For this analysis, the nominal sideband region was chosen to be $1.135 < M_{p\pi} < 1.150$

GeV/c^2 , but the effects of varying this region are studied in detail in the next chapter. The $r_{\text{comb.}}$ is the integral of the combinatorial background in the $C_{\text{signal}}^{\text{h-p}\pi}$ distribution, obtained by

$$r_{\text{Comb}} \equiv \frac{B}{S + B} \int \int C_{\text{signal}}^{\text{h-p}\pi}(\Delta\varphi, \Delta\eta) d\Delta\varphi d\Delta\eta, \quad (3.9)$$

where S and B are the signal and background obtained from the fits to the Λ invariant mass distributions in Figure 3.7. As the S/B ratio is the same for the Λ invariant mass distributions in events with a trigger hadron as it is for the h- Λ distributions, the scale $B/(S + B)$ can be used to give only the background contribution from the integral $\int \int C_{\text{signal}}^{\text{h-p}\pi}(\Delta\varphi, \Delta\eta) d\Delta\varphi d\Delta\eta$. The self-normalized $C_{\text{SB, norm.}}^{\text{h-p}\pi}$ distribution is then scaled by $r_{\text{comb.}}$ and subtracted from $C_{\text{signal}}^{\text{h-p}\pi}$ to remove the combinatorial background.

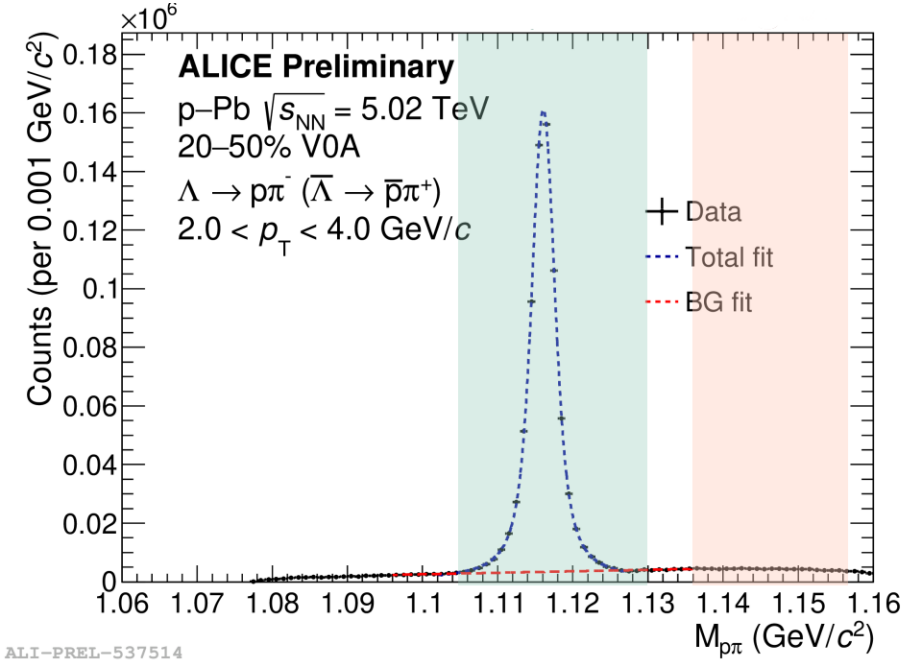


Figure 3.14: Invariant mass distribution of $p\pi$ pairs in the 20-50% multiplicity class. The signal region is shown in light green, and the sideband region is shown in light pink. The correlation distribution in the sideband region is used to remove the combinatorial background from the signal region.

While the above procedure describes the background removal in a more technical manner, it can be condensed into the following steps:

1. Generate the correlation distribution using Λ candidates in the signal invariant mass region

2. Do the same thing for Λ candidates in the sideband invariant mass region
3. Scale the sideband distribution to match the background in the signal region
4. Subtract the sideband distribution from the signal distribution

Examples of the signal and sideband distributions $C_{\text{signal}}^{\text{h-p}\pi}$ and $C_{\text{SB}}^{\text{h-p}\pi}$ are shown for the 0-20% multiplicity bin in Figure 3.15.

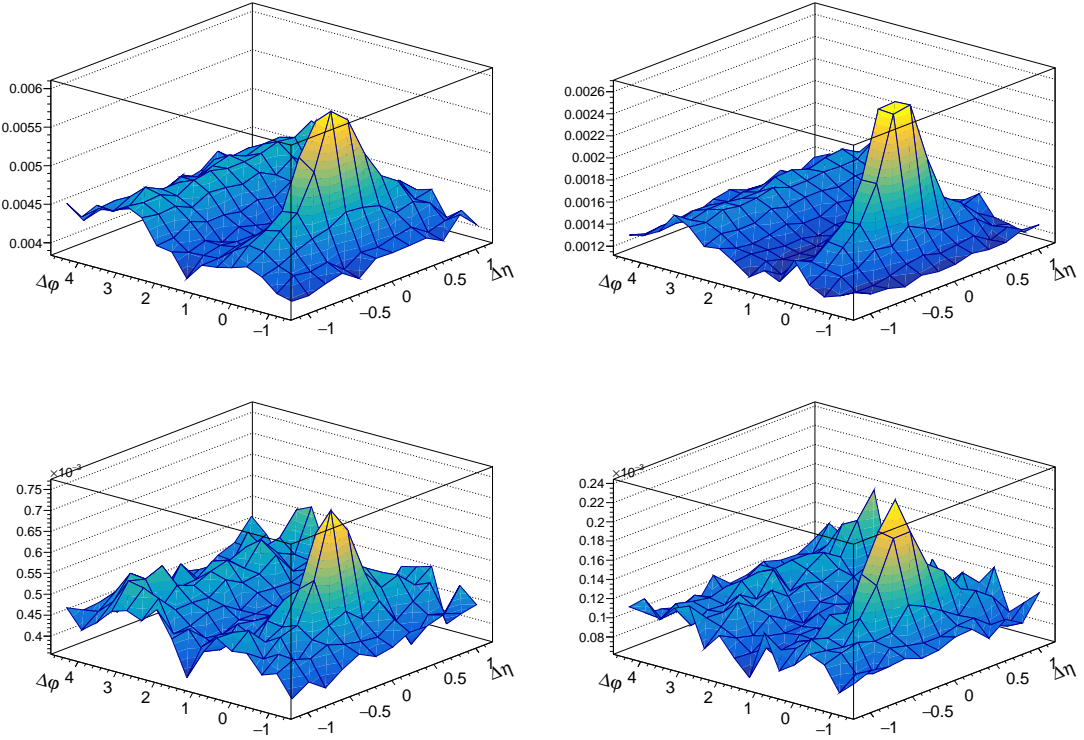


Figure 3.15: The signal (top) and sideband (bottom) distributions $C_{\text{signal}}^{\text{h-p}\pi}$ and $C_{\text{SB}}^{\text{h-p}\pi}$ for the lower (left) and higher (right) associated p_T bins. All plots were generated in the 0-20% multiplicity class.

3.5.3.2 Signal scaling

As the Λ candidate invariant mass signal region is finite, the fraction of the Λ signal that is missed in the tails of the invariant mass distribution must be corrected for.

This is handled by the r_{signal} term in Equation 3.7, which is calculated by

$$r_{\text{signal}} \equiv \left(\frac{\text{Integral of residual in signal region}}{\text{Integral of residual between 1.098 and 1.134}} \right)^{-1} \quad (3.10)$$

where ‘‘residual’’ refers to the invariant mass distributions from Figure 3.7 after subtracting the straight-line background fit. 1.098 and 1.134 are the points in which there is effectively zero signal, verified in Monte Carlo. Due to the width of the signal region, r_{signal} is usually near unity. However, to study the effects of narrowing the signal region, this term must be included in the analysis.

3.5.3.3 Branching ratio correction

The most simple correction from Equation 3.7 comes from the branching ratio term, namely

$$r_{\text{branch}} \equiv \frac{1}{BR(\Lambda \rightarrow p\pi)} = \frac{1}{0.639}. \quad (3.11)$$

As not all Λ s decay into $p\pi$ pairs, this term corrects for the fraction of Λ s that decided to decay into something else. In many analyses, this term is not required as it is already included in the efficiency computation $\epsilon_{\text{assoc.}}$. As the Λ reconstruction efficiency from this analysis is calculated using only Λ s that decay into $p\pi$ pairs, this term must be included separately.

3.5.3.4 Pair efficiency correction

The ϵ_{pair} term in Equation 3.7 is the h- Λ ‘‘pair’’ efficiency, which is used to correct for track merging effects. Many correlation studies are susceptible to track merging inefficiencies [13], [14], whereby either the trigger or associated particle gets merged over by the other during the track reconstruction. This results in a dip at small angles in the angular correlation distribution when compared to a similar distribution with no instances of track merging. As this effect cannot be seen directly in data due to the missing reconstructed tracks, it is investigated using the Monte Carlo sample, where the reconstructed tracks are compared to the MC-generated particles they were reconstructed from. While this effect is usually negligible and only relevant at extremely small angles ($\Delta\varphi < 0.01, \Delta\eta < 0.1$), in this analysis this effect is more severe and occurs at larger angles ($\Delta\varphi < 1, \Delta\eta < 0.6$), shown in Figure 3.16.

The severity of this effect for the h- Λ distributions is likely due to two factors:

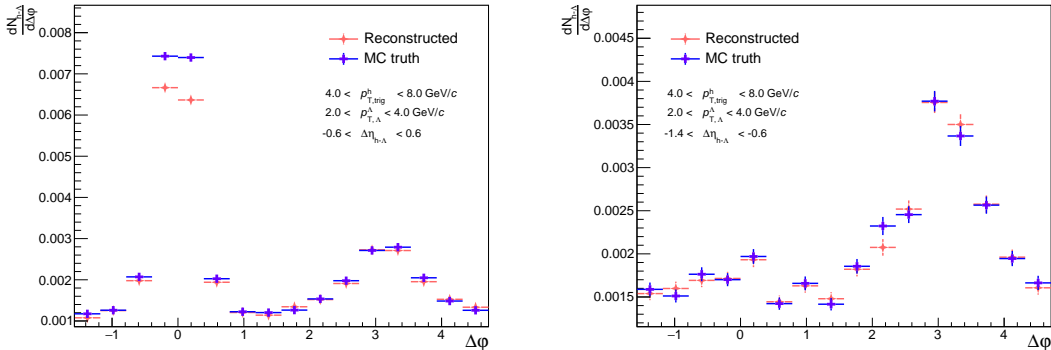


Figure 3.16: Demonstration of the track merging effect for h- Λ pairs, whereby we see a dip in the reconstructed distribution at small $\Delta\varphi$ and $\Delta\eta$ when compared to the MC ground truth (left). This dip is not present at large $\Delta\eta$ (right), but we also lose nearly the entirety of our near-side peak.

- The Λ decay length is large ($c\tau \approx 10$ cm), meaning the daughter particles will have less hits in the detector than the trigger particle (which is produced at the primary vertex). As Kalman filtering (track reconstruction) favors the track with more hits, the Λ daughter track is “merged” over by the trigger track.
- The Λ decay is asymmetric ($m_p/m_\pi \approx 7$), so the Λ and daughter proton end up with similar momenta (and thus φ and η). This means that whenever a proton from a Λ decay is “merged” over by a trigger track, a h- Λ pair with small $\Delta\varphi, \Delta\eta$ is lost.

To see how the decay length can affect the track merging, the (reconstructed)/(MC ground-truth) $C(\Delta\varphi, \Delta\eta)$ distribution ratio for h-pion pairs in our MonteCarlo sample where the pion is **secondary**—meaning it came from a weak decay with decay length > 2 cm—is measured. Pions are chosen for this demonstration as they are more abundantly produced than protons, and charged track reconstruction is particle species agnostic. Any “dips” from unity present in this ratio are indicative of pairs being lost during reconstruction. This is then compared to the same ratio for h-pion pairs where the pion is **primary**, and the results are shown in Figure 3.17. All reconstructed triggers and pions pass the trigger hadron and Λ daughter cuts from Tables 3.2 and 3.4, respectively. Furthermore, all distributions have been fully corrected for single-particle efficiencies and detector acceptance using the procedures

from Sections 3.5.1 and 3.5.2, respectively. A large suppression at small $(\Delta\varphi, \Delta\eta)$ is observed for the h-secondary pion case, but the h-primary pion case exhibits no such suppression. As such, it stands to reason that this suppression is at least in part due to the decay length of the Λ , as all particles that come from Λ s are secondaries (by a long shot).

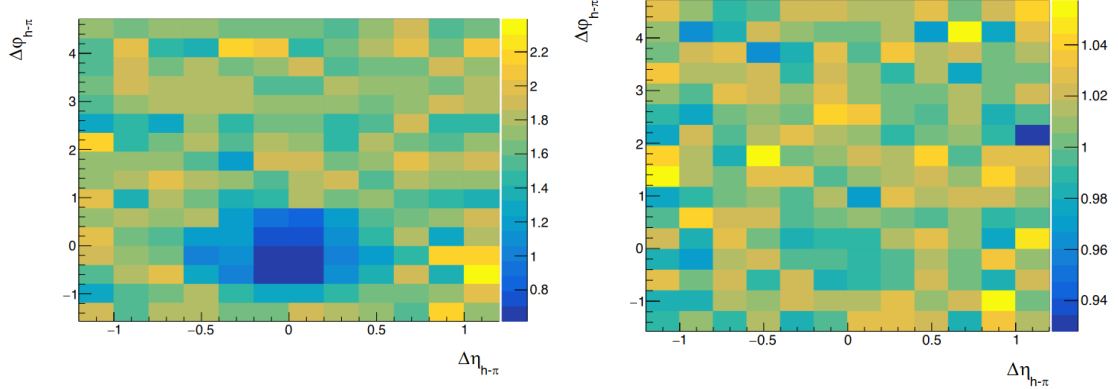


Figure 3.17: The reconstructed/ground truth ratios of the 2D $C(\Delta\varphi, \Delta\eta)$ distributions for h-(secondary pions) (left) and h-(primary pions) (right). The suppression at smaller $\Delta\varphi, \Delta\eta$ is clearly seen in the secondary case, but is not observable in the primary case, indicating a decay-length dependence.

The p_T dependence of this effect can also be studied by measuring the reconstructed and ground truth h -(secondary pion) $\Delta\varphi$ distributions at low ($1.0 < p_T < 2.0$ GeV/c) and high ($2.0 < p_T < 4.0$ GeV/c) associated momentum. The result is shown in Figure 3.18. Note that the distributions were projected onto $\Delta\varphi$ with $|\Delta\eta| < 1.2$. A suppression relative to MC ground-truth is observed in the near-side of the reconstructed distribution in the higher p_T range, which is not seen in the low p_T bin. This is also consistent with the decay length dependence shown in the previous figures, as decay length is roughly proportional to p_T .

The p_T dependence of this inefficiency demonstrates why this effect is so severe in the h- Λ case: due to the asymmetry of the Λ decay ($m_p/m_\pi \approx 7$), the daughter proton receives most of the momentum. Therefore when investigating h- Λ correlations within a given associated p_T range, any inefficiencies present in the corresponding h-(daughter proton) distribution with the same associated momentum would also be present in our final h- Λ distribution within a similar $\Delta\varphi, \Delta\eta$ range. As demonstrated in Figure 3.18, secondary charged particles with $2 < p_T < 4$ GeV/c see a large

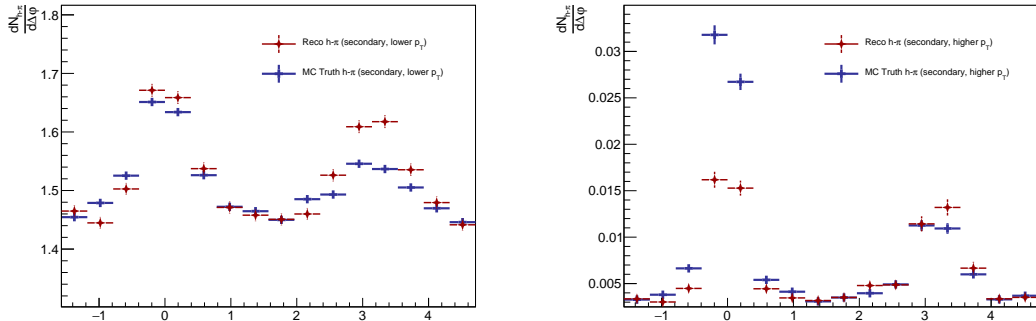


Figure 3.18: The reconstructed and ground truth $\Delta\varphi$ distributions in the $-1.2 < \Delta\eta < 1.2$ region for h-(secondary pions) with $0.15 < p_T < 2$ (left) and $2 < p_T < 4$ (right). The suppression at smaller $\Delta\eta, \Delta\varphi$ is clearly seen in the higher momentum bin, but not present in the lower one.

inefficiency, and therefore we would expect a similar inefficiency to be present in our $h-\Lambda$ distribution (which was shown in Figure 3.16). In similar analyses using the K_S^0 in lieu of the Λ [15], such an effect is not as present, both because the decay length is much shorter (2 cm vs 10 cm), and the K_S^0 decay is symmetric, meaning the daughter pions will have momenta that are no longer similar to the mother kaon.

The following techniques have been investigated to correct for this effect:

- Applying a $\Delta\varphi^*$ correction, described in **DphiStar**: While $\Delta\varphi$ and $\Delta\varphi^*$ are different, they are correlated enough that in order to remove this effect, a $|\Delta\varphi^*| < 0.7$ cut is required, which removes a significant amount of the near-side yield in the corresponding $\Delta\varphi$ distribution.
- Applying a cut on the minimum distance between the fully reconstructed helices of the trigger and Λ daughter proton (varied between 0.1 cm and 10 cm): Again, this cut removes roughly the same amount of near-side yield as the $\Delta\varphi^*$ cut, as this minimum distance is also highly correlated with $\Delta\varphi$.
- Using the resonance technique for Λ reconstruction (more details in Section ??): this moderately reduces the severity of this effect, but the statistical fluctuations introduced by the smaller S/B ratio make it difficult to gauge how effective this correction is.

- Only correlating h- Λ pairs where the charge of the Λ daughter proton (or antiproton) is opposite to the trigger, as oppositely charged tracks bend in opposite directions in the detector magnet: This reduces the effect by a considerable amount, but reduces our overall correlation statistics by a factor of 2.
- Selecting “lower quality” trigger tracks by loosening the cuts from Table 3.2 so they are less likely to be merged over the low-quality daughter tracks: this reduces the effect, but introduces a large amount of secondary contamination. Furthermore, we would like this analysis to be directly compared with other analyses, and therefore want to maintain the same cuts on the trigger hadron.
- Selecting “higher quality” Λ daughter tracks by tightening the cuts from Table 3.4 (and adding additional selection criteria): this again reduces the effect but heavily cuts into the Λ signal

As each of these techniques reduces the statistics of the h- Λ correlation distribution beyond the realm of acceptability, the two-track inefficiencies are instead corrected for using a MC-generated template method, similar to the one used in [14]. For this method, the pair efficiency is given by

$$\epsilon_{pair}(\Delta\varphi, \Delta\eta) \equiv \frac{C_{\text{reco}}^{\text{tag}}(\Delta\varphi, \Delta\eta)}{C_{\text{gen}}(\Delta\varphi, \Delta\eta)}, \quad (3.12)$$

where $C_{\text{reco}}^{\text{tag}}$ is the efficiency-corrected correlation distribution calculated in MC using reconstructed trigger hadrons and Λ candidates with the same selection criteria as described in Section 3.2, with the additional requirement that the Λ candidate has a corresponding generated Λ which is used for all calculations involving kinematic quantities. This removes the need to perform any of the additional corrections from the previous sections (e.g. background subtraction, signal scaling) as the invariant mass of generated lambdas is exact. C_{gen} is the correlation distribution calculated in MC using only generated trigger hadrons and Λ candidates. The template $\epsilon_{pair}(\Delta\varphi, \Delta\eta)$ is applied for each associated p_T bin in this analysis, but it is independent of multiplicity and event generator. The templates for each associated p_T bin are shown in Figure 3.19. This correction is applied to the h- Λ distributions after side-band subtraction, signal scaling and the branching ratio correction.

After these corrections, both the h- Λ and h-h 2D distributions are finalized and ready for projection onto $\Delta\varphi$ to extract the yields and widths of interest from the

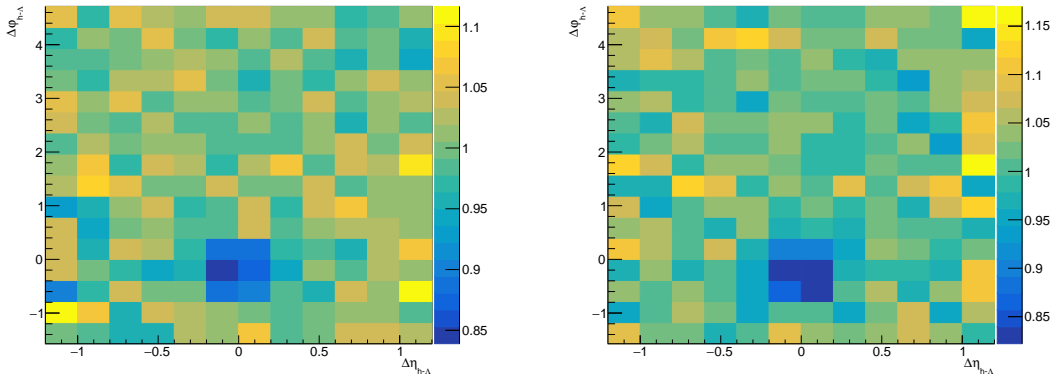


Figure 3.19: The $\epsilon_{\text{pair}}(\Delta\varphi, \Delta\eta)$ templates for the track merging correction in the lower ($1.5 < p_T < 2.5$ GeV/ c , left) and higher ($2.5 < p_T < 4.0$ GeV/ c , right) associated momentum bins. While it may be difficult to observe, the lower p_T bin has a minimum dip of around 0.84, whereas the higher p_T bin has a minimum dip of around 0.81, reflecting the p_T dependence discussed in this section.

previous chapter. However, there are still a number of systematic uncertainties to investigate and cross-checks required to ensure the validity of the final results.

Chapter Four: Systematic uncertainties and cross-checks

Systematic uncertainties are inevitable in any analysis, and the present one is no exception. This chapter describes the various sources of systematic uncertainties that affect the final results, and how their magnitudes are estimated and propagated to the final uncertainties. This chapter also presents the cross-checks that were performed to verify the robustness and consistency of the analysis, and to ensure that no biases were introduced along the way.

4.1 Systematic uncertainties

“The treatment of systematic errors is often mishandled. This is due to lack of understanding and education, based on a fundamental ambiguity as to what is meant by the term”

—Roger Barlow, *Systematic Errors: Facts and Fictions* [16]

In every experimental analysis, choices must be made. These choices can be as simple as the selection of a particular data set, or as complex as choosing a fit function of fifteen parameters instead of three. In either case, these choices can have an effect on the final results, which is quantified by the **systematic uncertainty**. Broadly speaking, the systematic uncertainty is a measure of the sensitivity of the final results to the choices made during the analysis procedure.

In this analysis, the procedure for estimating the systematic uncertainty from a certain choice is as follows:

1. Vary the choice in a way that is reasonable and justifiable
2. Measure the observable of interest after the variation
3. Quantify the effect of the variation on the observable by calculating the percent change from the original value of the observable
4. Vary the choice in a slightly different way, and repeat steps 2 and 3

5. Repeat steps 2 through 4 until all reasonable variations have been considered
6. Calculate the systematic uncertainty as the root mean square (RMS) of the percentages from step 3.

Note the usage of the words “reasonable” and “justifiable”, which seem to indicate that the systematic uncertainty is a subjective quantity. Indeed the process of obtaining the systematic uncertainty involves even more choices, like the choice of which choices to consider, the choices of how to vary the choices, and even the choice on how to quantify the uncertainty itself. In this sense, the systematic uncertainty is a moderately subjective quantity, where the analyzer must use their best judgement to determine which choices are indeed reasonable. To that end, the list of sources of systematic uncertainties considered for this analysis is not exhaustive, but it is the best attempt at a comprehensive list of reasonable choices that affect the final results.

To provide more structure to this section, the analysis procedure is broken into the following components:

1. The generation of the $h-\Lambda$ and $h-h$ $\Delta\varphi$ distributions,
2. The extraction of the pairwise yields from the $\Delta\varphi$ distributions, and
3. The extraction of the near- and away-side widths from the fits of the $\Delta\varphi$ distributions,

which are used to separate this section into three subsections, one for each of these components. In each section, the sources of systematic uncertainties are described, followed by a Barlow analysis [16] to ensure the variations result in a statistically significant deviation from the nominal values. Finally, a summary of the final systematic uncertainties is provided.

4.1.1 $\Delta\varphi$ distribution generation

The sources of systematic uncertainties that affect the $\Delta\varphi$ distribution considered for this analysis are the following, in order of decreasing magnitude:

- Λ topological selection ($h-\Lambda$ distribution only)
- Material budget

Table 4.1: The systematic uncertainties for the $\Delta\varphi$ distributions which are not directly calculated in this thesis, instead taken from previous analyses using the same particle species and collision system [15], [17]–[19]. Each source of uncertainty is verified to be independent of multiplicity, but the Λ material budget and topological selection uncertainties exhibit a small dependence on p_T .

Source name	Lower p_T %	Higher p_T %
Λ topological selection	3.2%	3.0%
Λ material budget	1.1%	0.6%
Charged h tracking efficiency	3.5%	3.5%
Charged h material budget	negl.	negl.

- Tracking efficiency
- Λ daughter PID cuts ($h-\Lambda$ distribution only)
- Λ invariant mass signal region selection ($h-\Lambda$ distribution only)
- Λ invariant mass sideband region selection ($h-\Lambda$ distribution only)

As the Λ topological selection, material budget, and tracking efficiencies have been studied in detail in previous analyses using the same particle species and collision system [15], [17], [18], the systematic uncertainty associated with these sources is taken directly from these analyses and presented in Table 4.1. The uncertainties from these sources exhibit no multiplicity dependence, and a very small dependence on p_T . These uncertainties are also assumed to be independent of $\Delta\varphi$, although this is studied more thoroughly in Section ??.

Each of the other sources of systematic uncertainty is described in detail in the following sections.

4.1.1.1 Signal region selection

The nominal signal region for the Λ invariant mass is fairly wide, accounting for nearly 97% of the total Λ signal. However, the final result should not be heavily influenced by the choice of signal region so long as it is centered about the true Λ mass. Furthermore, altering the signal region tests the validity of the signal scaling procedure outlined in Section 3.5. To investigate this, the signal region is varied in the ways presented in Table 4.2. The resulting $\Delta\varphi$ distributions and ratios to the nominal distribution for each signal region variation in each multiplicity and associated p_T bin

are shown in Figures 4.1 (lower p_T) and 4.2 (higher p_T). The average deviation from the nominal distribution is around 2%, with no individual variation exceeding 5%. As no significant dependence on $\Delta\varphi$ is observed, the systematic uncertainty is calculated as the RMS of the percent change from each variation across the entire $\Delta\varphi$ range as opposed to calculating the RMS in each bin.

Table 4.2: The variations of the Λ invariant mass signal region considered for this analysis.

Variation name	Signal range (GeV/c^2)
Narrow	$1.108 < M_{p\pi} < 1.124$
Narrower	$1.112 < M_{p\pi} < 1.120$
Wide	$1.100 < M_{p\pi} < 1.132$
Wider	$1.096 < M_{p\pi} < 1.136$

4.1.1.2 Sideband region selection

The choice of sideband region also leaves a lot of room for reasonable variation: all that is required is that the region is 1) large enough to produce a smooth h-p π distribution with minimal statistical fluctuations and 2) close enough to the signal region that the p π pairs are kinematically similar to those in the background of the signal region. As long as these requirements are met, the final result should not be very dependent on the choice of sideband region. To investigate the effects of changing the sideband region, the variations presented in Table 4.3 are considered. The measured $\Delta\varphi$ distributions and variation/nominal ratios for each sideband region variation in each multiplicity and associated p_T bin are shown in Figures 4.3 (lower p_T) and 4.4 (higher p_T). The result is even less deviation from the nominal distribution than the signal region variations, with the average deviation being closer to 1%. Again, no significant dependence is observed on $\Delta\varphi$, so the systematic uncertainty is calculated as the RMS of the percent change from each variation across every $\Delta\varphi$ bin.

4.1.1.3 Λ daughter particle identification

The Λ daughter particle identification (PID) cuts are chosen to be wide enough to ensure a high efficiency, but narrow enough to ensure a high purity. As the requirement for a higher purity should be offset by the subtraction of the combinatorial

Table 4.3: The variations of the Λ invariant mass sideband region considered for this analysis. Note that the “shifted left” sideband falls on the opposite (left) side of the signal region.

Variation name	Sideband range (GeV/c^2)
Narrow	$1.135 < M_{p\pi} < 1.145$
Wide	$1.135 < M_{p\pi} < 1.16$
Shifted left	$1.086 < M_{p\pi} < 1.098$
Shifted right	$1.14 < M_{p\pi} < 1.155$

background, altering the PID cuts should only minimally effect the final $\Delta\varphi$ distributions. To study this, the PID cuts are varied in the ways presented in Table 4.4. The final $\Delta\varphi$ distributions and ratios to the nominal distribution for each PID cut variation in each multiplicity and associated p_T bin are shown in Figures 4.5 (lower p_T) and 4.6 (higher p_T). Requiring a signal in the TOF detector drastically reduces the Λ signal as the daughter pions are often heavily deflected by the magnetic field due to their lower p_T (again, $m_p/m_\pi \approx 7$, so most of the mother momentum belongs to the proton). This causes a large amount of statistical fluctuations in the corresponding $\Delta\varphi$ distribution, which is why the “require TOF” variation is inevitably excluded after the Barlow check presented in Section 4.1.1.4. The other variations result in only around a 2% deviation from the nominal $\Delta\varphi$ distribution, on average.

Table 4.4: The variations of the Λ daughter PID cuts considered for this analysis. The “require TOF” variation requires a TOF hit for both the proton and pion, but maintains the nominal values for $|n\sigma_{\text{TPC, TOF}}|$.

Variation name	$ n\sigma_{\text{TPC, TOF}}^\pi $	$ n\sigma_{\text{TPC, TOF}}^p $
Narrow	< 1.8	< 1.2
Wide	< 4.2	< 2.8
Require TOF	< 3.0	< 2.0

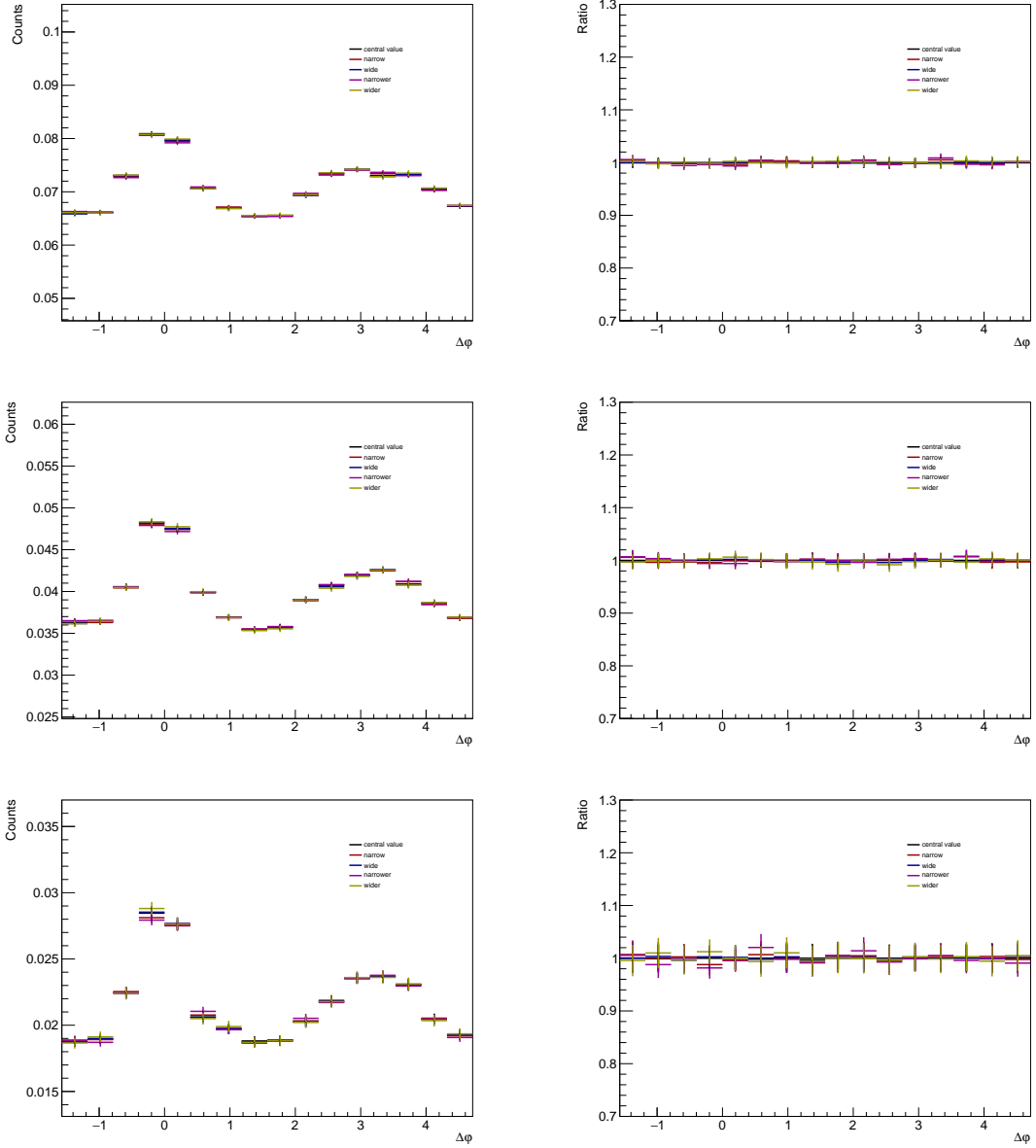


Figure 4.1: The $h-\Lambda$ $\Delta\varphi$ distributions within the 0-20% (top), 20-50% (middle) and 50-80% (bottom) multiplicity bins in the lower associated p_T bin for each of the signal region variations (left) with the ratios to the nominal distribution (right).

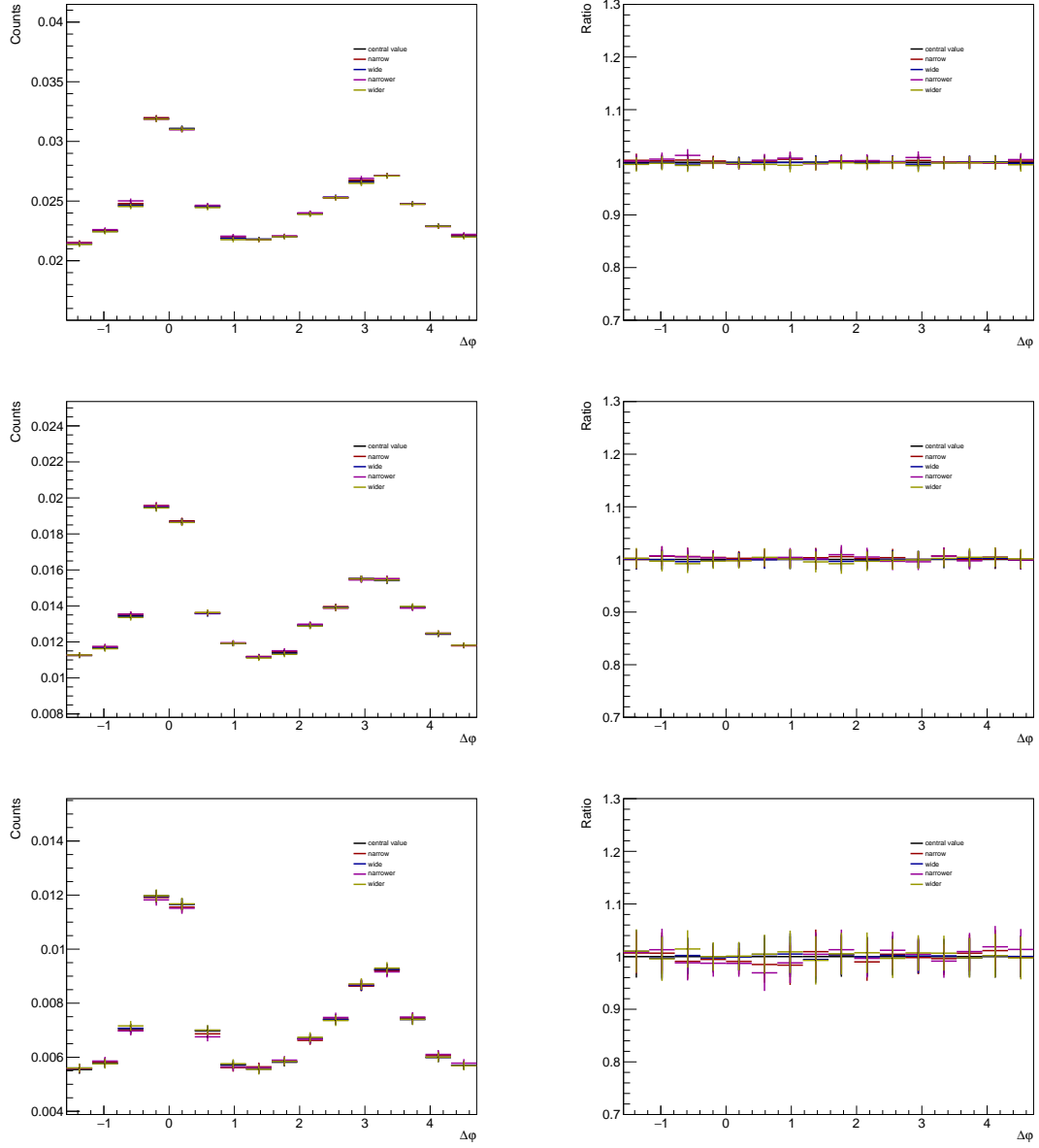


Figure 4.2: The $h-\Lambda$ $\Delta\varphi$ distributions within the 0-20% (top), 20-50% (middle) and 50-80% (bottom) multiplicity bins in the higher associated p_T bin for each of the signal region variations (left) with the ratios to the nominal distribution (right).

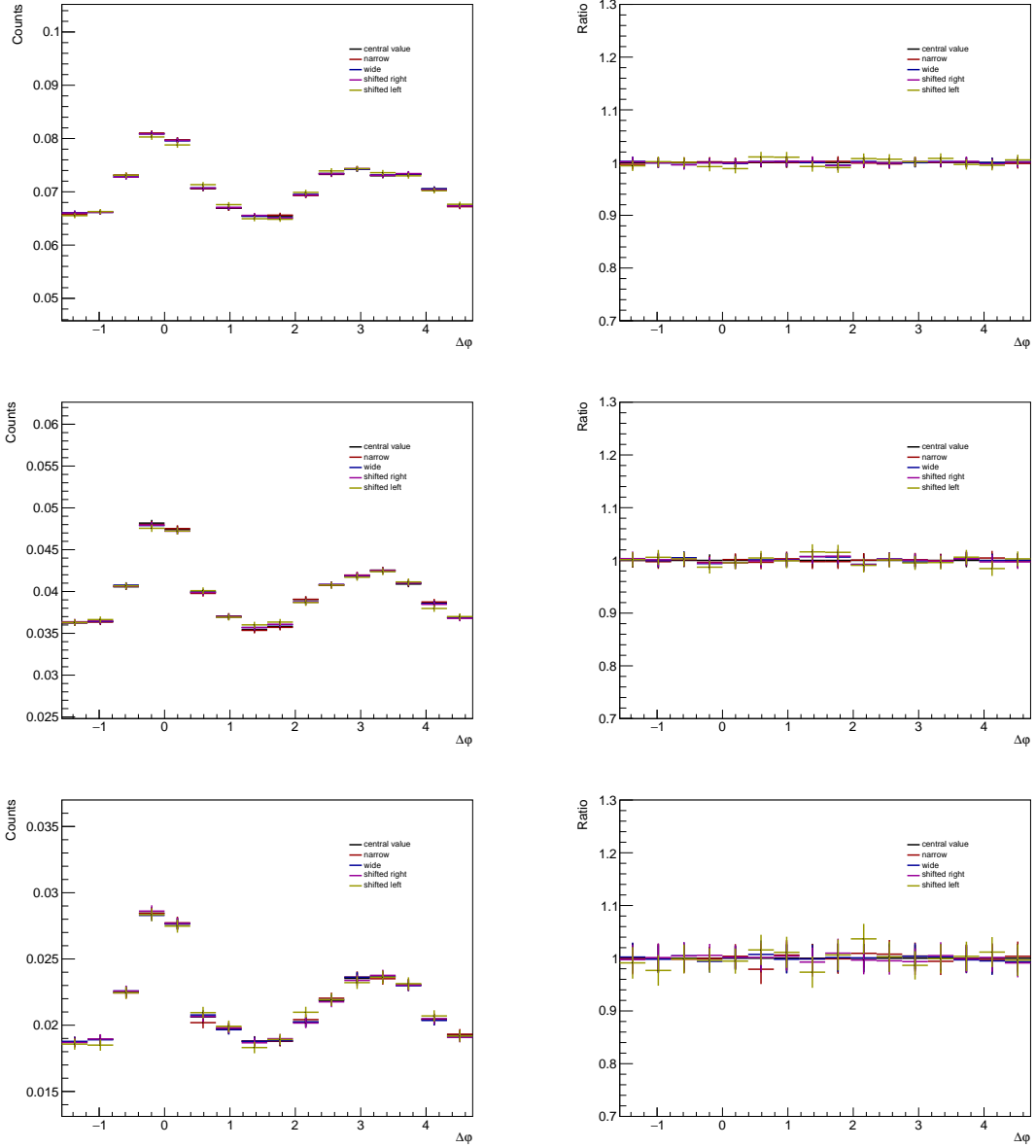


Figure 4.3: The $h-\Lambda$ $\Delta\varphi$ distributions within the 0-20% (top), 20-50% (middle) and 50-80% (bottom) multiplicity bins in the lower associated p_T bin for each of the sideband region variations (left) with the ratios to the nominal distribution (right).

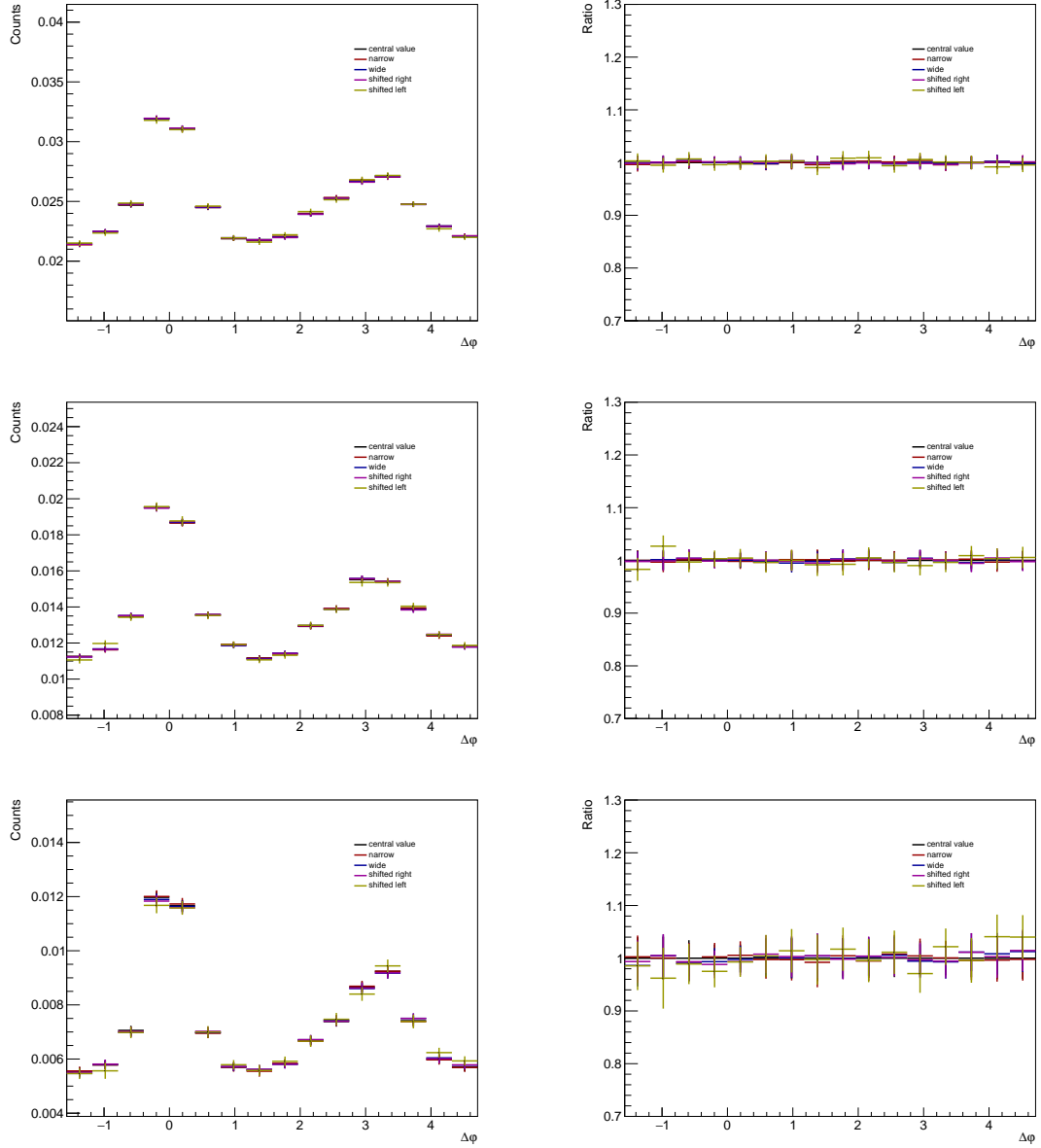


Figure 4.4: The $h-\Lambda$ $\Delta\varphi$ distributions within the 0-20% (top), 20-50% (middle) and 50-80% (bottom) multiplicity bins in the higher associated p_T bin for each of the sideband region variations (left) with the ratios to the nominal distribution (right).

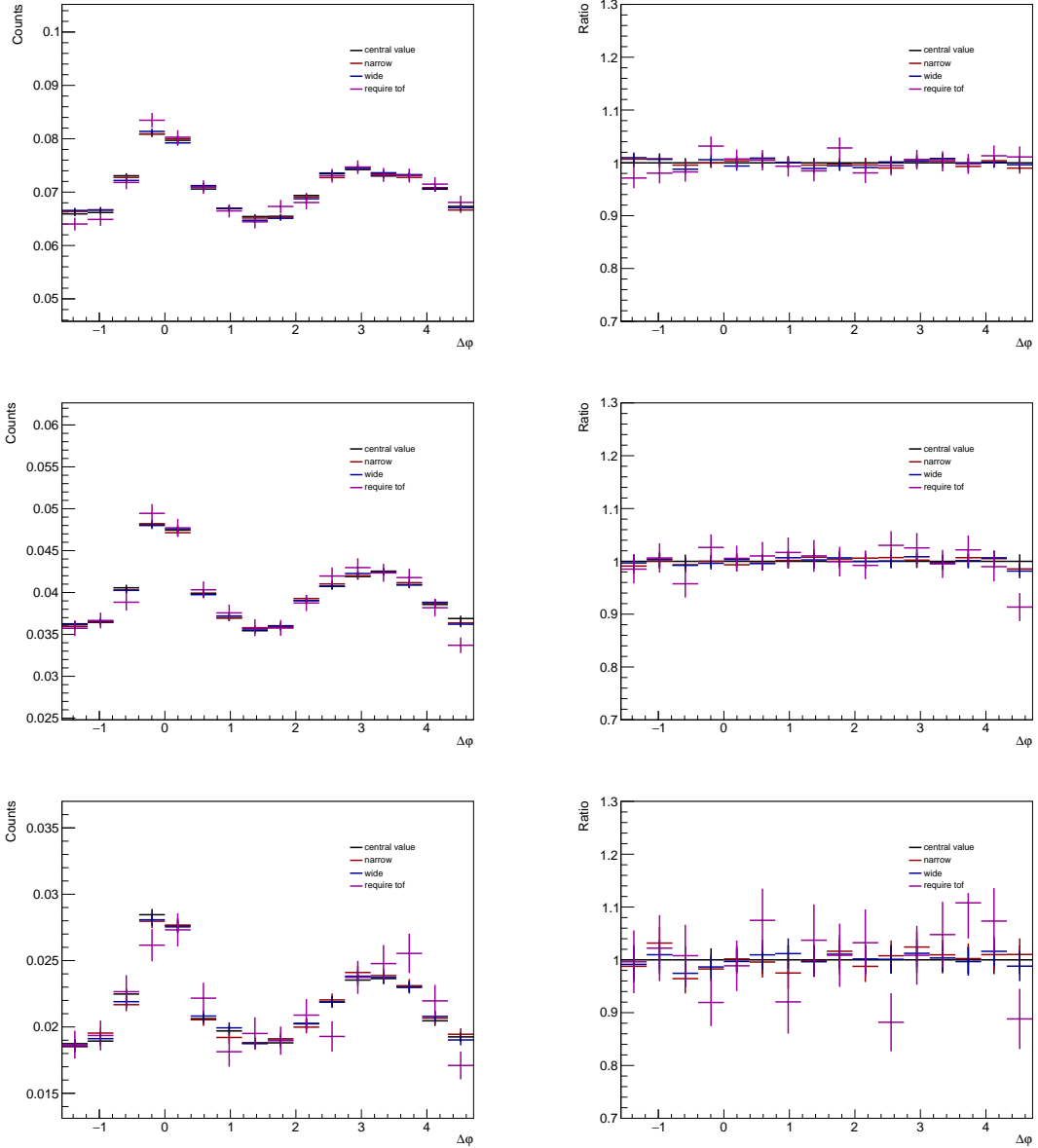


Figure 4.5: The $h-\Lambda$ $\Delta\varphi$ distributions within the 0-20% (top), 20-50% (middle) and 50-80% (bottom) multiplicity bins in the lower associated p_T bin for each of the PID cut variations (left) with the ratios to the nominal distribution (right).

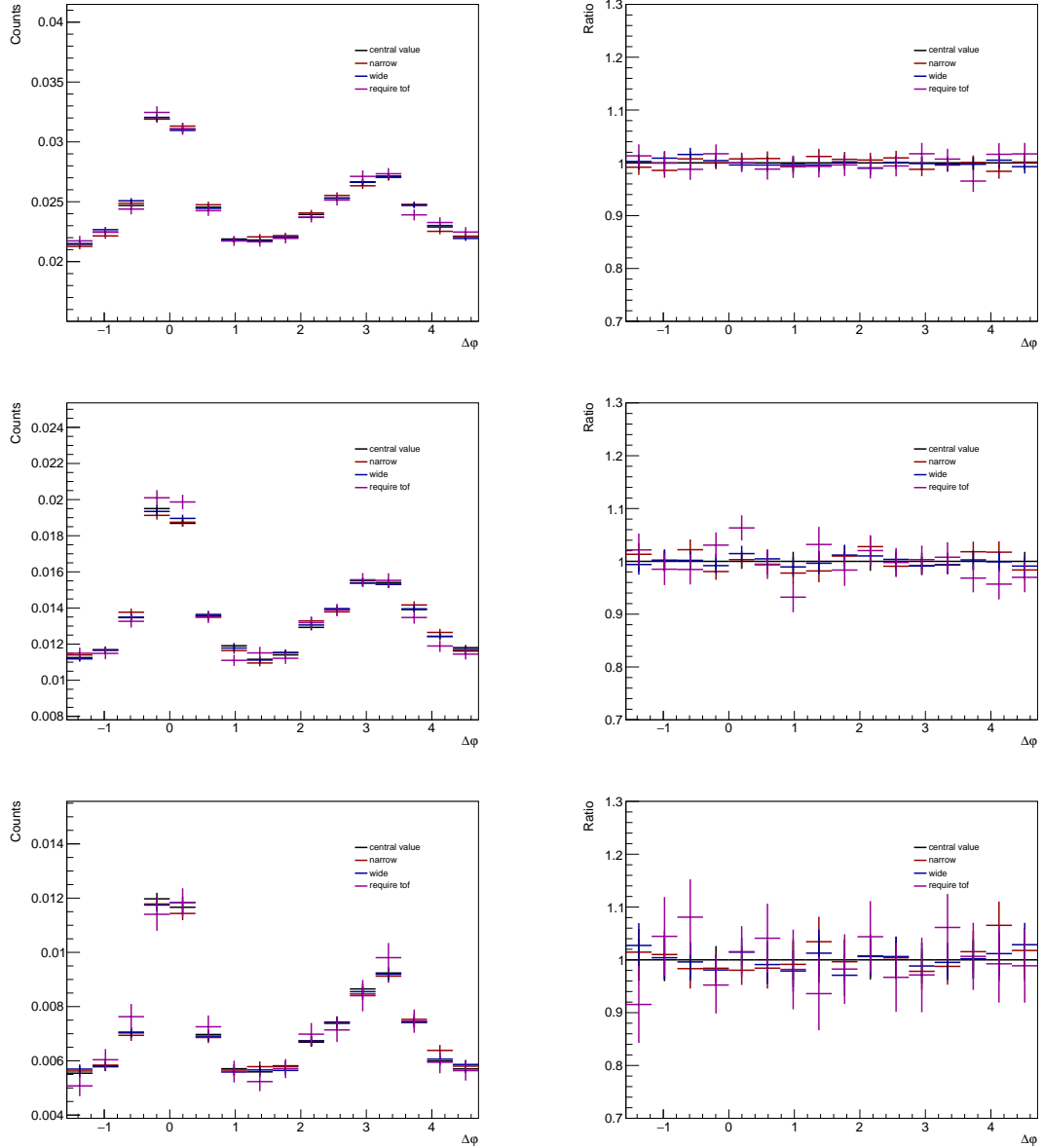


Figure 4.6: The $h-\Lambda$ $\Delta\varphi$ distributions within the 0-20% (top), 20-50% (middle) and 50-80% (bottom) multiplicity bins in the higher associated p_T bin for each of the PID cut variations (left) with the ratios to the nominal distribution (right).

4.1.1.4 Barlow check for $\Delta\varphi$ distribution uncertainties

Due to statistical fluctuations, it may be the case that some variations result in a statistically insignificant deviation from the nominal $\Delta\varphi$ distribution. In such cases, the variation should not be considered in the final systematic uncertainty calculation. To determine which variations give statistically significant deviations, a Barlow check [16] is performed. For each $\Delta\varphi$ bin, the following quantity is calculated:

$$N\sigma_{RB} := \frac{y_{\text{var.}} - y_{\text{nom.}}}{\sqrt{|\sigma_{\text{var.}}^2 - \sigma_{\text{nom.}}^2|}}, \quad (4.1)$$

where $y_{\text{var.}}$ and $\sigma_{\text{var.}}$ are the measured yield and statistical uncertainty for the variation, and $y_{\text{nom.}}$ and $\sigma_{\text{nom.}}$ are the yield and statistical uncertainty for the nominal value.

To determine whether a given variation should be excluded, the number $\Delta\varphi$ bins that have $|N\sigma_{RB}| < 1$ is counted. If this is the majority of the bins (across all multiplicity and associated p_T ranges), the variation is excluded from the systematic calculation. Example plots of $N\sigma_{RB}$ for each variation of the signal, sideband and PID cuts are shown in Figure 4.7. The red lines represent $N\sigma_{RB} = \pm 1$.

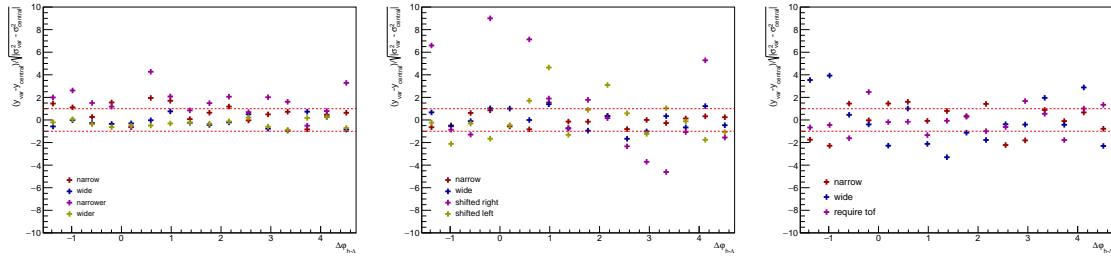


Figure 4.7: Barlow check for the signal (left), sideband (middle), and PID (right) variations in the 0-20% multiplicity bin. The red lines represent $N\sigma_{RB} = \pm 1$, and if the majority of the points fall within the red lines (across all $\Delta\varphi$, multiplicity and p_T bins), they are excluded from the systematic uncertainty calculation.

As a result of the check, the following variations are excluded from the final systematic uncertainty calculation:

- Signal: wide, wider
- Sideband: wide, narrow

- PID: require TOF

These exclusions are not so surprising. As the nominal signal region is already fairly wide, making it wider does not significantly change the $\Delta\varphi$ distribution. Similarly, the initial sideband region falls fairly close to the signal region. So long as there are enough statistics in the corresponding sideband h- Λ distribution, changing its width should not affect the $\Delta\varphi$ distribution in a meaningful way. It also appears that requiring a TOF hit introduces large statistical errors, which dominate the denominator in Equation 4.1.

4.1.1.5 Final systematic uncertainties for $\Delta\varphi$ distributions

The final systematic errors (after the Barlow check) from the h- Λ $\Delta\varphi$ distribution generation for each multiplicity bin and p_T bin are shown in Table 4.5. The total systematic uncertainty is calculated by adding each systematic error in quadrature. This table is consolidated into plots showing the systematic errors for each multiplicity bin and p_T bin, which are presented in Figure 4.8. As the systematic uncertainties associated with the generation of the dihadron $\Delta\varphi$ distributions are only from the tracking efficiency presented in Table 4.1, they are not plotted in this section.

Table 4.5: The final systematic uncertainties (in percentages) from the h- Λ $\Delta\varphi$ distribution generation for each multiplicity and associated p_T bin.

Mult. and p_T bin	Sig.	Sideband	PID	Topo. sel.	Mat. bud.	Total
0-20%, low p_T	0.36	0.53	0.64	3.2	1.1	3.3
20-50%, low p_T	0.35	0.67	0.65	3.2	1.1	3.4
50-80%, low p_T	0.76	1.1	1.4	3.2	1.1	3.8
0-20%, high p_T	0.42	0.42	0.76	3.0	0.6	3.2
20-50%, high p_T	0.4	0.71	1.2	3.0	0.6	3.3
50-80%, high p_T	1.1	1.6	2.0	3.0	0.6	4.1

The total systematic error is observed to be mostly p_T -independent. However, there appears to be a slight correlation between the systematic uncertainty and multiplicity, with the 0-20% bin exhibiting lower uncertainties than the 50-80% bin across both p_T ranges. This can become problematic when investigating the multiplicity dependence of observables extracted from the $\Delta\varphi$ distributions, as the fraction of the systematic uncertainty which is directly correlated with multiplicity should not be considered when measuring multiplicity-dependent trends like slopes and percent

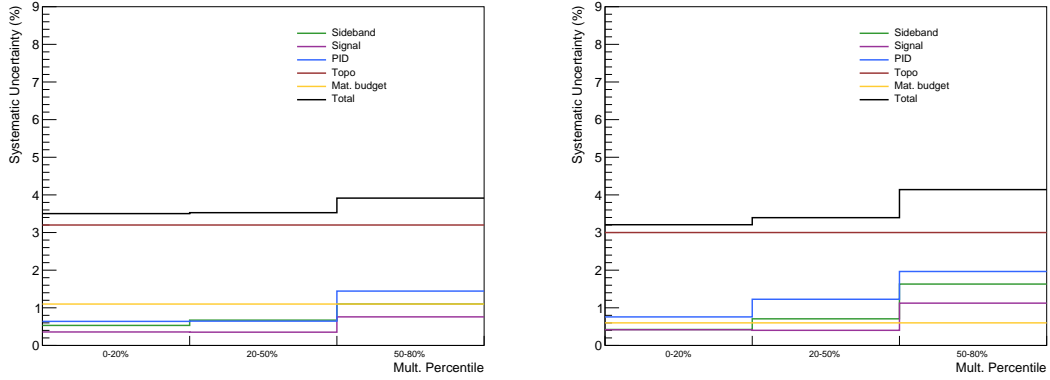


Figure 4.8: A visual depiction of the final systematic errors for the $h\Lambda \Delta\varphi$ distributions for each multiplicity bin in the low (left) and high (right) associated p_T bins. The total systematic error is shown in black.

changes. Because of this, the fraction of the systematic uncertainty which is uncorrelated with multiplicity is approximated using

$$\sigma_{\text{uncor},i}^2 = \sum_{\text{vars}} (R_{\text{var},i} - 1)^2, \quad (4.2)$$

where

$$R_{\text{var},i} = \left(\frac{y_{\text{var},i}}{y_{\text{nom},i}} \right) / \left(\frac{y_{\text{var}}^{\text{MB}}}{y_{\text{nom}}^{\text{MB}}} \right), \quad (4.3)$$

where “i” refers to the i th multiplicity bin, and “MB” refers to the min-bias (multiplicity-integrated) results. The deviations of $R_{\text{var},i}$ from unity quantify how the deviations in multiplicity bin i differ from those in the MB sample. $\sigma_{\text{uncor},i}$ is computed for each $\Delta\varphi$ bin, then the RMS is taken across all $\Delta\varphi$ bins to obtain the final multiplicity-uncorrelated portion of the systematic errors. The results for each p_T bin are shown in Figure 4.9. These systematic errors are only used when quantifying the multiplicity dependence of an observable extracted from the $\Delta\varphi$ distributions.

4.1.2 Yield extraction

The largest source of systematic uncertainty of this analysis corresponds to the different techniques that can be used to extract the yields in the near-side jet, away-side jet and underlying event from the $\Delta\varphi$ distributions. As mentioned in Section ??, the

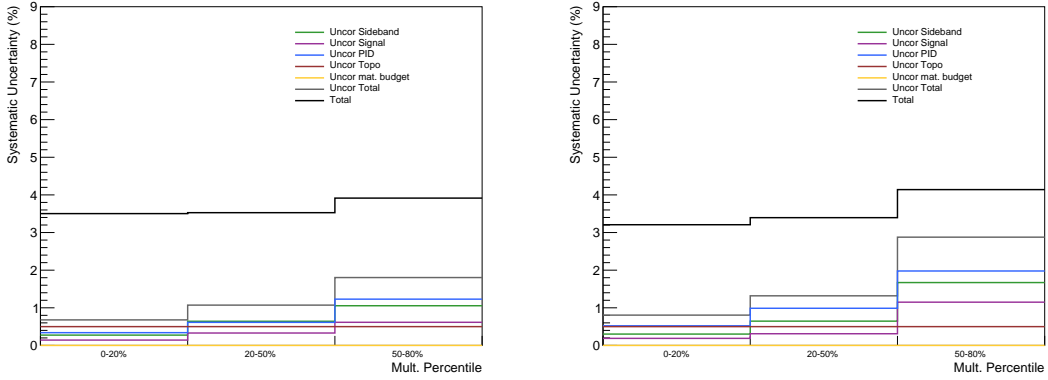


Figure 4.9: Visual depiction of the multiplicity-uncorrelated systematic errors for the $h\Lambda \Delta\varphi$ distributions for each multiplicity bin in the low (left) and high (right) associated p_T bins, along with the total systematic error shown in black.

equations for extracting these yields are

$$Y_{near} = \int_{-\pi/2}^{\pi/2} \left(\frac{dN}{d\Delta\varphi} - U(\Delta\varphi) \right) d\Delta\varphi, \quad Y_{away} = \int_{\pi/2}^{3\pi/2} \left(\frac{dN}{d\Delta\varphi} - U(\Delta\varphi) \right) d\Delta\varphi \quad (4.4)$$

$$Y_{UE} = \int_{-\pi/2}^{3\pi/2} U(\Delta\varphi) d\Delta\varphi, \quad (4.5)$$

where $\frac{dN}{d\Delta\varphi}$ is the $\Delta\varphi$ distribution and $U(\Delta\varphi)$ is the underlying event fit. These equations naturally introduce two categories of systematic uncertainty: those associated with the underlying event fit, and those associated with the integration of the $\Delta\varphi$ distribution.

4.1.2.1 Underlying event fit techniques

As the underlying event term $U(\Delta\varphi)$ is present in every yield extraction equation above, any changes in the underlying event fitting procedure will affect the final yield measurements. To maintain compatibility with previous analyses (specifically for the dihadron correlations), the nominal underlying event fit is a straight line to the average of the $\Delta\varphi$ distribution in the ranges $[-\frac{\pi}{2}, -\frac{\pi}{4}] \cup [\frac{\pi}{4}, \frac{5\pi}{8}] \cup [\frac{11\pi}{8}, \frac{3\pi}{2}]$. These ranges were initially chosen as there is expected to be little-to-no contamination from the jet components in each range. However, to investigate the effect the UE fitting procedure may have on the final yields, the following alternative methods were considered:

1. Straight line fit in a more restricted range, specifically $[-\frac{\pi}{2}, -\frac{3\pi}{8}) \cup [\frac{3\pi}{8}, \frac{5\pi}{8}) \cup [\frac{11\pi}{8}, \frac{3\pi}{2})$
2. Straight line fit using the Zero Yield At Minimum (ZYAM) technique, where the underlying event line is set to the minimum of the $\Delta\varphi$ distribution
3. Sinusoidal fit which includes a non-zero v_2 contribution

The first two techniques are similar enough to the nominal technique that they will not be explicitly shown in this section. However, the third technique requires new machinery to be developed, so it will be described in detail in the next section.

4.1.2.2 Including a non-zero v_2 contribution

For the final two techniques, we investigate the inclusion of a non-zero v_2 (which is definitely the case, especially in our 0-20% multiplicity bin). First, the v_2 values are determined as a function of p_T from Figure 31 in this AN: https://alice-notes.web.cern.ch/system/files/notes/analysis/1228/2022-09-15-AN_PIDflowInSmallSystems_v4.pdf. As our p_T binning is much wider, we then take the weighted average across each of our p_T bins using the published p_T spectra for charged hadrons and Λ s from HEPData (found here: <https://www.hepdata.net/record/ins1244523?version=2>). The final values in the 0-20% multiplicity bin for each $p_{T,assoc}$ bin are shown in Table 4.6.

$p_{T,assoc}$	$v_2^{trigger}$	$v_2^{assocch}$	$v_2^{assoc\Lambda}$
2.0 - 4.0	0.092	0.112	0.111
1.5 - 2.5	0.092	0.100	0.075
2.5 - 4.0	0.092	0.119	0.137

Table 4.6: v_2 values used in this analysis for each $p_{T,assoc}$ bin.

As there is no data available for the 20-50% and 50-80% multiplicity bins, we take 0.85 and 0.5 times the 0-20% value, respectively.

Using these v_2 values, we then fit the following function to the $\Delta\varphi$ distribution in the regions $-\pi/2 < \Delta\varphi < -1$ and $1 < \Delta\varphi < +\pi/2$ (i.e., regions with little-to-no jet components). The fit function is given by:

$$Fit_{v_2}(\Delta\varphi) = A \times (1 + 2v_{2,trig}v_{2,assoc}\cos(2\Delta\varphi)) \quad (4.6)$$

where A is the underlying event pedestal, which is allowed to vary during the fit. The v_2 values are fixed to the values in Table 4.6. The final two techniques both use the same fit function for the UE.

Bibliography

- [1] B. Pullman, *The Atom in the History of Human Thought*. Oxford: Oxford University Press, 1998, ISBN: 978-0-19-515040-7 (cit. on p. 1).
- [2] J. Dalton, “Experimental enquiry into the proportion of the several gases or elastic fluids, constituting the atmosphere,” *Memoirs of the Literary and Philosophical Society of Manchester*, vol. 1, pp. 244–258, 1805 (cit. on p. 1).
- [3] E. Rutherford, “The scattering of α and β particles by matter and the structure of the atom,” *Philosophical Magazine Series 6*, vol. 21, pp. 669–688, 1911 (cit. on p. 1).
- [4] J. Chadwick, “Possible existence of a neutron,” *Nature*, vol. 129, p. 312, 1932 (cit. on p. 1).
- [5] H. Kendall, *Deep inelastic scattering: Experiments on the proton and the observation of scaling*, 1990. [Online]. Available: <https://www.nobelprize.org/uploads/2018/06/kendall-lecture.pdf> (visited on 08/21/2023) (cit. on p. 1).
- [6] J. Friedman, *Deep inelastic scattering: Comparisons with the quark model*, 1990. [Online]. Available: <https://www.nobelprize.org/uploads/2018/06/friedman-lecture.pdf> (visited on 08/21/2023) (cit. on p. 1).
- [7] R. Taylor, *Deep inelastic scattering: The early years*, 1990. [Online]. Available: <https://www.nobelprize.org/uploads/2018/06/taylor-lecture.pdf> (visited on 08/21/2023) (cit. on p. 1).
- [8] R. P. Feynman, “The behavior of hadron collisions at the uncertainties from these sources exhibit no multiplicity dependence, and a very small dependence on p_T . extreme energies,” in *Special Relativity and Quantum Theory: A Collection of Papers on the Poincaré Group*, M. E. Noz and Y. S. Kim, Eds. Dordrecht: Springer Netherlands, 1988, pp. 289–304, ISBN: 978-94-009-3051-3. DOI: 10.1007/978-94-009-3051-3_25. [Online]. Available: https://doi.org/10.1007/978-94-009-3051-3_25 (cit. on p. 1).

- [9] S. Roesler, R. Engel, and J. Ranft, “The monte carlo event generator DPMJET-III,” in *Advanced Monte Carlo for Radiation Physics, Particle Transport Simulation and Applications*, Springer Berlin Heidelberg, 2001. arXiv: 0012252 [hep-ph] (cit. on pp. 11, 20).
- [10] A. Kalweit, *Energy loss calibration of the ALICE TPC*, 2008 (cit. on p. 14).
- [11] S. Acharya *et al.*, “Production of $K^*(892)^0$ and $\phi(1020)$ in pp and p–Pb collisions at $\sqrt{s_{NN}} = 5.02$ tev,” *Phys. Rev.*, vol. C97, 2022. doi: 10.1103/physrevc.106.034907. [Online]. Available: <https://doi.org/10.1103/physrevc.106.034907> (cit. on p. 18).
- [12] R. Brun *et al.*, *GEANT: Detector Description and Simulation Tool; Oct 1994*, ser. CERN Program Library. Geneva: CERN, 1993, Long Writeup W5013. doi: 10.17181/CERN.MUHF.DMJ1. [Online]. Available: <http://cds.cern.ch/record/1082634> (cit. on p. 20).
- [13] S. Acharya *et al.*, “Two-particle differential transverse momentum and number density correlations in p–Pb and Pb–Pb at the LHC,” *Phys. Rev. C*, vol. C100, no. 4, 2019. arXiv: 1805.04422 (cit. on p. 32).
- [14] ——, “Longitudinal and azimuthal evolution of two-particle transverse momentum correlations in Pb–Pb collisions at $\sqrt{s_{NN}} = 2.76$ TeV,” *Phys. Letters*, vol. B804, p. 135375, 2020. arXiv: 1910.14393 (cit. on pp. 32, 36).
- [15] ——, “ K_S^0 - and (anti-) Λ -hadron correlations in pp collisions at $\sqrt{s_{NN}} = 13$ TeV,” *The European Phys. Journal*, vol. C81, no. 10, 2021. arXiv: 2107.11209 [nucl-ex] (cit. on pp. 35, 40).
- [16] R. Barlow, *Systematic errors: Facts and fictions*, 2002. arXiv: 0207026 [hep-ex] (cit. on pp. 38, 39, 49).
- [17] S. Acharya *et al.*, “Multiplicity dependence of light-flavor hadron production in pp collisions at $\sqrt{s} = 7$ TeV,” *Phys. Rev.*, vol. C99, 2019. arXiv: 1807.11321 [nucl-ex] (cit. on p. 40).
- [18] B. A. et al., “Multiplicity Dependence of Pion, Kaon, Proton and Lambda Production in p–Pb Collisions at $\sqrt{s_{NN}} = 5.02$ TeV,” *Phys. Letters*, vol. B728, pp. 25–38, 2014. arXiv: 1307.6796 [nucl-ex] (cit. on p. 40).

- [19] B. Abelev *et al.*, “ K_S^0 and Λ production in Pb-Pb collisions at $\sqrt{s_{\text{NN}}} = 2.76$ tev,” *Phys. Rev. Lett.*, vol. 111, 2013. arXiv: 1307.5530 [nucl-ex] (cit. on p. 40).